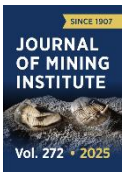
ISSN 2411-3336; e-ISSN 2541-9404

JOURNAL OF MINING INSTITUTE

Zapiski Gornogo instituta

Journal homepage: pmi.spmi.ru



Research article *Geology*

Paleoproterozoic Saltakh Pluton, Anabar Shield: mineralogical composition, age and a geodynamic setting

Nikolai I. Gusev[1, 2], **Lyudmila Yu. Romanova**[1, 2]✉

[1] *Karpinsky Russian Geological Research Institute, Saint Petersburg, Russia*

[2] *Institute of Precambrian Geology and Geochronology RAS, Saint Petersburg, Russia*

How to cite this article: Gusev N.I., Romanova L.Yu. Paleoproterozoic Saltakh Pluton, Anabar Shield: mineralogical composition, age and a geodynamic setting. Journal of Mining Institute. 2025. Vol. 272. N 16344, p. 16-39.

Abstract

The Saltakh Massif is located in the northern Anabar Shield, in the Saltakh shear-zone. It consists of two-pyroxene schists and plagiogneisses metamorphosed under granulite-facies conditions. Their chemical composition is consistent with that of a differentiated series of rocks ranging from gabbro to tonalites with abundant alaskitic gneissose granite veins and bodies. The rocks are mainly high-potassium ($K_2O/Na_2O > 0.50$), high-magnesium (mg# 50-70), low-titanium (TiO_2 0.35-1.31 wt.%) with low TiO_2 concentration in clino- and orthopyroxene. Normative olivine makes up 6-9 % of metagabbroic rocks. The rocks display well-defined negative Ti, Nb, Ta, and P anomalies typical of subduction magmatism. The two-pyroxene gneisses show high Sr/Y ratios of 67.6-88 and $(La/Yb)_N$ of 24.8-25.6. Saltakh rocks are part of a shoshonite series, as indicated by Nb/La, La/Yb, Th/Nb and Ce/Yb ratios. All the rocks display positive $\varepsilon_{Nd}(T)$ values of 1.9-4.1 and $\varepsilon_{Sr}(T)$ of 0.77-17.8 indicative of a mantle source of magma and $T_{(Nd)}$DM of 2,20-2,26 Ga. U-Pb zircon dating (SHRIMP II) has shown that the protoliths of Saltakh melanocratic rocks were dated at 2100-2086 Ma, and those of two-pyroxene plagiogneisses of tonalite composition were dated at 2025±7 Ma. Alaskitic gneissose granites were dated at 1969±7 Ma. The study of the trace element composition of zircon has revealed general enrichment in LREE. High LREE concentrations are due to secondary zircon alterations and the shoshonitic pattern of the melt, the high-temperature conditions of crystallization, and an anomalous fluid regime. The geodynamic setting in which the Saltakh Massif was formed was consistent with a pericontinental magmatic arc. The formation of alaskitic gneissose granites was due to anatexis provoked by later collision processes. Saltakh magmatic rocks were formed simultaneously with magmatic rocks from the Khapchan prospect which occur farther south, and were studied earlier (2095±10 Ma tholeiitic metadiorites and 2030±17 Ma calc-alkaline metatonalites). We interpret them as part of a metamorphosed juvenile Paleoproterozoic suprasubduction complex.

Keywords

Anabar Shield; Saltakh Massif; granulites; U-Pb method; geochronology

Funding

Studies were conducted under Russian Science Foundation project N 23-27-00098.

Received: 10.11.2023 ***Accepted: 02.05.2024*** ***Online: 26.08.2024*** ***Published: 25.04.2025***

Introduction

The Siberian Craton is an old platform with an Early Precambrian highly metamorphosed basement located in the northern part of the Eurasian continent. The Anabar Shield, consisting of granulitic terrains, forms a basement scarp in the northeastern Siberian Craton. Extending in the eastern Anabar Shield is the boundary of two Precambrian basement provinces: the Archean Anabar province and the Paleoproterozoic Olenek province formed of the Khapchan foldbelt. The Saltakh complex is located in the Popigai Terrane within the Olenek province. Its massif lies in the northern Saltakh shear-zone.

The Saltakh shear-zone extends in the northeastern Anabar Shield across the upper reaches of the River Staraya, the Popigai terrain and the right-hand bank of the River Nalim-Rassokha (Fig.1) [1]. The visible length of the zone is about 130 km. In the north and south, it is overlain by Riphean sandstones. The zone varies in width from 1-2 km in the south to 17-20 km in the north [2].

This is an open access article under the CC BY 4.0 license

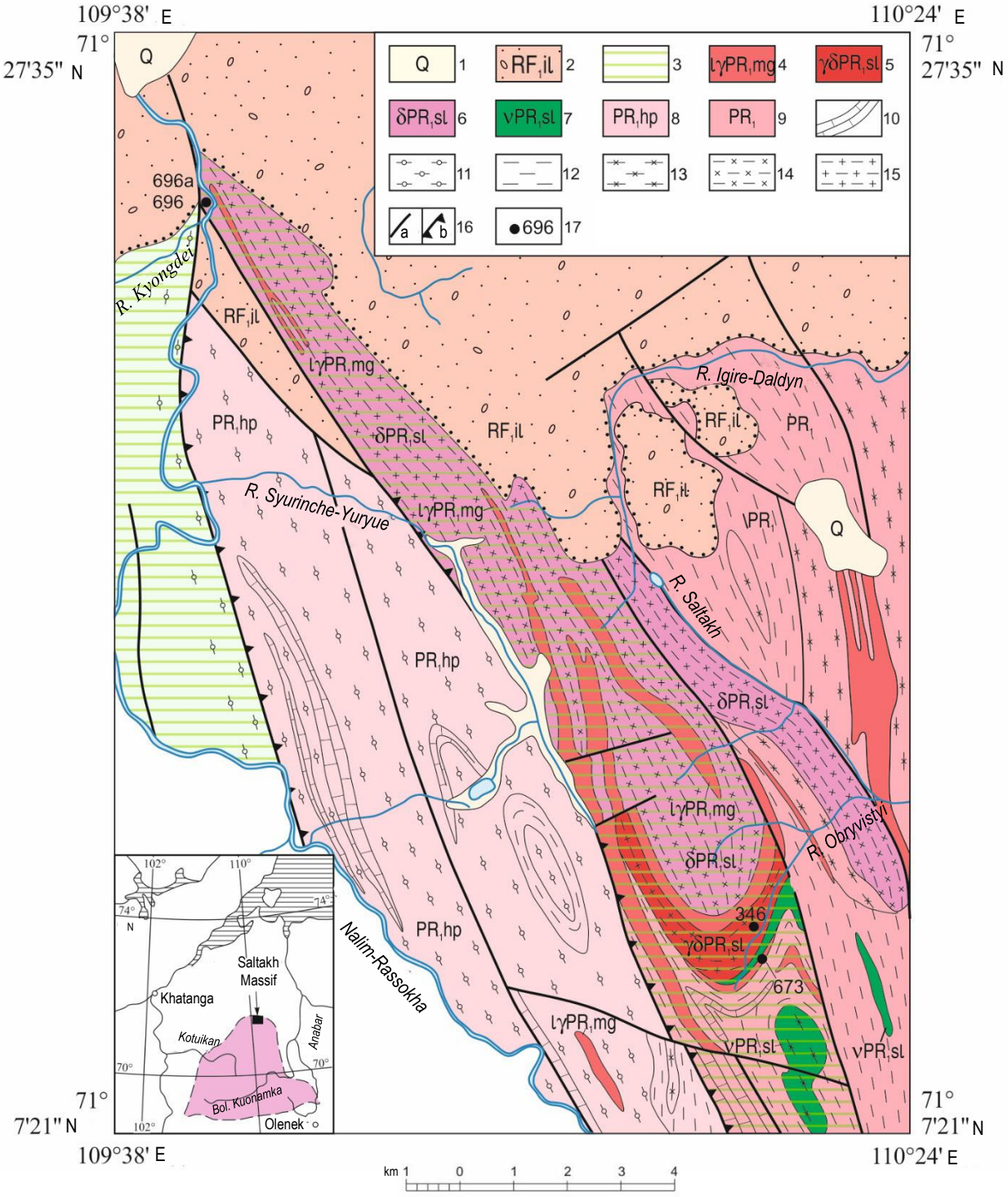


Fig.1. Geologic map of the Saltakh Massif area. Based on Gosgeolmap-200 (A.I.Trukhalev et al., 1972, unpublished data), modified

1 – Quaternary deposits (Q); 2 – red sandstones and gritstones of the Ilyinsk suite (RF_1il); 3 – broken down and retrogressed granulites in shear-zones; 4 – Magan alaskitic-leucogranitic-migmatitic complex ($l\gamma PR_1mg$); 5-7 – Saltakh gabbro-dioritic-tonalitic complex (ν, δ, γδ PR_1sl): 5 – two-pyroxene plagiogneisses (metatonalites), 6 – two-pyroxene gneisses (metadiorites), 7 – two-pyroxene schists (metagabbroic rocks); 8 – Khapchan series (PR_1hp): garnet, biotitic-garnet, garnet-pyroxene and sillimanite-garnet paragneisses, silicate marbles, carbonate-silicate and pyroxene-scapolitic rocks; 9 – undivided Paleoproterozoic (PR_1) rocks: orthopyroxene and two-pyroxene gneisses and plagiogneisses, mesocratic and mafic schists; 10 – silicate marbles, carbonate-silicate and pyroxene-scapolitic rocks; 11 – garnet, hypersthene-garnet gneisses, plagiogneisses and their varieties with biotite and graphite; 12 – hypersthene, two-pyroxene and amphibole-pyroxene plagiogneisses; 13 – clinopyroxene-plagioclase, two-pyroxene-plagioclase and amphibole-pyroxene-plagioclase schists; 14 – mesocratic orthogneisses and plagioschists; 15 – two-pyroxene plagiogneisses; 16 – boundaries: a – steeply dipping faults, b – overthrusts; 17 – sampling sites and the numbers of samples for isotopic analyses

This is an open access article under the CC BY 4.0 license

The Saltakh complex consists of two large massifs: the Saltakh Massif (covering an area of 10 × 24 km, including its northeastern satellite) and the Ulkhan Massif (2 × 20 km), as well as 10 smaller lenticular metagabbronorite intrusive units identified during the compilation of the Gosgeol-200 Map in 1971-1972 (A.I.Trukhalev et al., 1972, unpublished). The intrusive units of the Saltakh complex extend northwest for 100 km, varying in width from 10 km in the north to 20 km in the south. Metaintrusive rock exposures are more massive, but the boundaries of the massifs are indistinct, because their rocks have experienced granulite-facies metamorphism. Transitions to the host gneisses and schists are generally gradual. Zones of cataclasis and mylonitization are often formed along the contacts. Banding and stratification in the Saltakh Massif dip at 40-60° from the centre to the periphery of the massif [2].

Salltakh rocks have been metamorphosed along with host rocks under granulite-facies conditions. Most of these rocks contain hypersthene with antiperthitic feldspar. Transitions from the highly granitized host plagiogneisses and crystalline schists to Saltakh rocks are gradual [3]. Stretching along the western pluton boundary is the Saltakh diaphthoresis zone with amphibolite-facies polymetamorphic rocks, migmatites and alaskites [3]. Migmatization in the massif is widespread. It is intersected by numerous lenticular biotitic and alaskitic granite bodies, which vary in thickness (up to 0.5-0.9 km) and length (from several meters to tens of kilometers). The alaskitic granite bodies are affected by cataclasite zones, but they themselves are not cataclastic and are conformable with the western and southern massif boundaries. We have studied two prospects in the Saltakh Massif: one in the north, downstream from the Kyongdei River mouth, and the other in the southern zone of the massif extending along the banks of the Obryvistyi River (Fig.1). In the northern part of the massif, the rocks have been more intensely subjected to cataclasis, while in the southern part, the rocks are better preserved.

Methods

Major elements concentrations in the rocks were calculated by XRF methods, while ferric and ferrous iron concentrations were measured by titration and trace element concentrations by ICP-MS in the Karpinsky Institute laboratory, St.Petersburg.

Zircon samples were subjected to U-Pb dating using a SHRIMP II ion microprobe at the CIS, Karpinsky Institute, St.Petersburg (analyzed by P.A.Lvov) following standard methods [4]. The data obtained were processed with SQUID software (K.Ludwig, 2000). U-Pb ratios were normalized to the value 0.0668 for the TEMORA zircon standard dated at 416.75 Ma [5]. Errors in single analyses (ratios and ages) are given at the 1σ level, and errors in the calculated values of concordant ages and intersections with the Concordia curve are given at the 2σ level. Plots were constructed using ISOPLOT/ET software (K.Ludwig, 1999).

Trace elements in zircon were analyzed using ICP-MS method on a Cameca IMS-4f ion microprobe at the Yaroslavl Branch of the Institute of Physics and Technology, RAS. The study is described in detail in [6]. Data on the trace element composition of the zircon enabled us to reconstruct its conditions of formation [7-9] and to correctly interpret the dating results [10-12].

Rb-Sr and Sm-Nd isotope studies were conducted using the method described in [13]. Isotopic measurements were made on a ThermoFinnigan MAT TRITON mass-spectrometer (CIS, Karpinsky Institute, analyzed by E.S.Bogomolov) in a static regime.

To calculate $\varepsilon_{Nd}(T)$ values, we used the following modern isotopic ratios for a homogeneous chondritic reservoir (CHUR): $^{147}Sm/^{144}Nd = 0.1967$ and $^{143}Nd/^{144}Nd = 0.512638$ [14]. A model age for a one-stage model of $T_{Nd}(DM)$ was calculated relative to relatively depleted mantle (DM) with the parameters $^{147}Sm/^{144}Nd = 0.2136$ and $^{143}Nd/^{144}Nd = 0.51315$ [15]. Mineral symbols are used as per [16].

Results

Geologic-petrographic description. We have identified three rock groups in the Saltakh Massif study areas: two-pyroxene schists (metagabbroic rocks); two-pyroxene and orthopyroxene gneisses (metadiorites and metatonalites); and granitoids.

Two-pyroxene schist – their texture is generally massive and chaotically gneissoid (flaser). Cataclastic varieties display a banded texture. Thin sections are dominated by a granoheteroblastic structure, and a relict gabbroic structure persists locally. We identified two rock varieties:

This is an open access article under the CC BY 4.0 license

in one variety, the concentration of plagioclase is either equal to or less than that of dark-colored minerals, while in the other, plagioclase is clearly dominant.

The melanocratic varieties of the schist samples analyzed show the following mineral composition, vol.%: Pl (An_{45-58}) 45-50, Cpx 20-25, Opx 5-10, Bt 10-25, Mag 4, Ilm 1, Ap 1. Leucocratic schist varieties have the following mineral composition, vol.%: Pl (An_{40}) 55-60, Cpx 15, Opx 5, Bt 18-20, Mag 4, Ilm 1, Ap 1.

Plagioclase often forms isometric grains with fractured margins and no twinning. The granulated mass occasionally contains superposed quartz and K-feldspar. Plagioclase occurs mainly as andesine-labradorite. Bitownite is occasionally present (An_{72}) in the Ulkhan Massif, where original rocks are better preserved.

Clinopyroxene of the diopside-hedenbergitic series forms irregular isometric grains and often replaces orthopyroxene. Clinopyroxene crystals generally contain the decay structures and twins of solid solutions with thin orthopyroxene laminae. TiO_2 concentration in the clinopyroxene is as low as 0.06-0.25 wt.% [2].

Orthopyroxene occurs as hypersthene and bronzite, which display pleochroism in pink tones, forming irregular and short-prismatic grains. Orthopyroxene is replaced by clinopyroxene, biotite, and amphibole with magnetite grains. It contains less TiO_2 (0.02 wt.%) than clinopyroxene [2]. Apatite is regularly distributed, forming isomorphic grains often showing hexagonal cross-sections.

A distinctive feature of two-pyroxene gneisses is the presence of antiperthitic plagioclase, quartz and orthopyroxene, which dominates over clinopyroxene. Their mineral composition vol.%: Pl (An_{30-35}) 55-70, Qz 10-15, Opx 6-10, Cpx 4-5, Bt 5-10, Or 0-8, Mag 2, Ilm 1, Ap 0.5.

Red-coloured gneissose granites (sample 347) show the following mineral composition vol.%: Kfs 35, Pl (An_{20-30}) 30, Qz 28-30, Bt 3, Mag 1. Single coarse grains occasionally contain Ap and Ttn, Zrn, and less often Mnz and Rt. Orthopyroxene, replaced by biotite and iddingsite, is occasionally present. Plagioclase is often antiperthitic and is corroded by quartz and orthoclase.

Alaskitic gneissose granites (sample 673) consist, vol.%: Kfs 37, Qz 32, Pl (An_{12}) 27. Microcline aggregates are commonly larger (1-3 mm across) than plagioclase. They often contain relics of myrmekitized plagioclase and orthoclase. Dark-coloured minerals are present as biotite and ore minerals such as magnetite and ilmenite. Articulate twins of rutile are occasionally derived from ilmenite. Grains of Ap, Zr, Mnz, and Aln are scarce.

Petro-geochemical types of rocks. The geochemical features of the rocks were studied based on 13 original analyses (Table 1). In addition, we used earlier evidence to understand better the petrochemical characteristics of the samples, such as 18 silicate analyses of two-pyroxene crystalline schists and gneisses (metadiorites) from the Saltakh Massif [2] and three analyses of crystalline schists (metagabbronorites) from the Ulkhan Massif. The Saltakh Massif [2] contains rocks ranging from monzogabbro to granodiorites, but as rock migmatization is ubiquitous, a TAS diagram can hardly be used. Since intermediate to mafic rocks prevail, our classification was based using all major rock constituents (Fig.2, *a*) and diagrams for the relations of relatively immobile high-charge elements Zr/Ti-Nb/Yb (Fig.2, *e*), equivalent to a TAS diagram (J.A.Pearce, 1996), and a Th-Co diagram (Fig.2, *f*), equivalent to a K_2O-SiO_2 diagram [17]. The correlation of normative feldspars was used for the classification of felsic rocks (Fig.2, *d*) [18].

The chemical composition of *two-pyroxene schist* (Table 1, Fig.2, *a*) is similar to that of gabbro (sample 672c, 672b), gabbronorite (Ulkhan Massif), and monzogabbro (samples 672, 672a, and 696). They are comparable in trace element concentration (Fig.2, *b*) to normal alkaline basaltoids. In the AFM diagram (Fig.2, *c*), the rocks are part of a calc-alkaline series. Earlier analyses indicated higher iron concentrations, which likely resulted from the distinctive analytical identification of elements by the wet chemistry method and a laboratory error.

The samples show a potassium type of alkalinity K_2O/Na_2O = 1.0-1.6, except for cataclastic rocks enriched in plagioclase with superposed quartz (sample 694-696, K_2O/Na_2O = 0.2-0.5). Figure 2, *f* shows that in Th-Co coordinates, all the rocks are part of a calc-alkaline series. However, it should be noted that Th is depleted during granulite-facies metamorphism. In the Ce/Yb-Ta/Yb diagram, the rocks are clearly plotted in the shoshonitic series, which separates calc-alkaline and shoshonitic series using the poorly mobile elements Ce, Yb and Ta (Fig.2, *h*) [19, 20].

This is an open access article under the CC BY 4.0 license

Journal of Mining Institute. 2025. Vol. 272. P. 16-39
© Nikolai I. Gusev, Lyudmila Yu. Romanova, 2024

Table 1

Contents of major (wt.%) and trace (ppm) elements in the rocks of the Saltakh Massif

Groups of rocks	Opx-Cpx shists					Cpx-Opx plagiogneisses						Gneissose granites	
Sample	672c	672b	672	672a	696	696a	695	696b	346	347a	694	347	673
SiO_2	50.9	50.7	51.6	50.8	53.0	62.4	63.4	66.3	62.3	64.6	68.2	70.2	75.2
TiO_2	0.88	0.89	1.29	1.31	1.16	0.92	0.72	0.69	0.49	0.35	0.57	0.23	0.01
Al_2O_3	11.3	11.4	16.3	16.4	18.0	16.1	15.9	15.3	16.4	16.8	14.9	15.5	13.9
Fe_2O_3	3.82	4.18	3.63	5.32	3.01	2.07	2.06	2.23	2.36	1.44	2.15	1.28	0.48
FeO	4.42	4.61	4.87	3.79	4.06	3.25	2.34	1.39	2.44	2.11	1.39	0.97	0.13
MnO	0.18	0.21	0.13	0.14	0.11	0.09	0.06	0.07	0.09	0.08	0.06	0.03	0.02
MgO	10.5	10.2	6.03	5.99	5.43	3.06	3.05	1.80	2.64	1.89	2.11	0.64	0.18
CaO	11.4	11.7	7.36	7.30	6.86	5.06	4.62	5.62	5.32	4.32	4.96	1.46	0.68
Na_2O	2.0	2.21	3.36	3.47	5.14	4.70	4.46	4.95	3.84	3.61	3.83	2.75	2.65
K_2O	2.89	2.29	3.46	3.41	1.67	1.39	2.13	0.79	2.64	3.60	0.70	6.05	6.27
P_2O_5	0.48	0.50	0.69	0.68	0.34	0.27	0.22	0.20	0.22	0.18	0.18	0.14	0.02
LOI	0.52	0.43	0.47	0.52	0.61	0.30	0.68	0.41	0.76	0.78	0.68	0,55	0.34
Total	99.29	99.32	99.19	99.13	99.39	99.61	99.64	99,75	99,50	99.76	99.73	99.80	99.72
Th	1.84	1.67	1.78	2.11	0.69	0.50	0.34	0.97	6.13	2.25	4.55	21.2	0.20
U	0.54	0,46	0.66	0.72	0.20	0.12	0.13	0.18	0.19	0.25	0.71	0.80	0.17
Rb	163	136	133	141	27.4	17.8	55.2	4.46	66.7	74.2	4.14	149	143
Cs	2.03	0.95	1.38	1.71	0.36	0.26	0.37	<0.1	0.27	0.22	0.11	0.27	0.22
Ba	1730	986	2210	2200	292	365	506	255	996	1120	80.9	1960	425
Sr	493	377	997	849	441	494	517	404	646	617	495	498	206
La	20.3	23.9	28.3	30.7	39.6	21.7	23.9	25.6	32.3	25.7	23.7	52.2	5.41
Ce	45.6	53.5	65.3	65	117	48.7	47.4	50.7	64.6	48.9	47.9	94.1	6.27
Pr	5.86	6.72	8.86	8.84	16.6	6.39	5.42	5.88	7.02	5.34	5.54	9.22	0,46
Nd	25	27	38.3	36.1	69.8	25.9	22.4	22.5	25.4	20.2	20.6	32.5	1.37
Sm	5.08	5.29	6.44	6.42	11.5	4.02	3.56	3.52	3.66	3.06	3.63	3.54	0.20
Eu	1.32	1.21	2.12	1.95	2.30	1.30	1.10	1.14	1.08	0.87	0.87	0.91	0.58
Gd	3.84	4.29	5.02	4.89	10	3.25	2.97	3.15	2.94	2.39	2.68	2.17	0.11
Tb	0.62	0.65	0.59	0.66	1.40	0.46	0.42	0.45	0.41	0.29	0.38	0.26	0.02
Dy	3.18	3.17	3.26	3.24	7.26	2.51	2.00	2.40	2.08	1.55	1.94	1.04	0.10
Ho	0.70	0.65	0.55	0.61	1.47	0.47	0.40	0.44	0.33	0.26	0.33	0.14	0.02
Er	1.59	1.74	1.36	1.52	3.99	1.12	1.07	1.12	1.03	0.70	1.06	0.33	0.05
Tm	0.24	0.24	0.21	0.22	0.64	0.20	0.13	0.17	0.14	0.11	0.16	0.06	0.01
Yb	1.67	1.63	1.61	1.43	4.16	1.26	1.01	1.20	0.85	0.70	0.84	0.47	0,09
Lu	0.19	0.26	0.17	0.21	0.57	0.18	0.14	0.15	0.15	0.12	0.15	0.05	0.01
ΣREE	115	130	162	162	286	118	112	118	142	110	110	197	14.7
Zr	117	99.2	132	132	213	165	154	159	110	125	141	241	21.2
Hf	3.61	3.24	3.28	3.30	5.48	3.99	3.42	3.61	2.88	3.09	3.71	5.97	0.88
Ta	0.33	0.41	0.44	0.47	0.92	0.49	0.35	0.90	0.14	0.21	0.91	0.05	0.05
Nb	5.68	6.46	8.32	8.44	16.5	9.19	6.53	9.46	4.13	4.73	8.61	2.05	0.25
Y	16.2	16.5	15.3	15.3	43.4	12.8	10.7	11.6	9.55	7.04	9.69	4.14	0.64
Cr	450	450	59.5	56.1	111	94.8	107	85.8	54.3	40.2	118	42.0	14.4
Ni	125	127	51.7	42.0	107	66.8	45.9	32.2	19.6	18.2	32.2	4.65	2.82
Co	44.5	48.6	35.5	36.7	25.5	17.0	15.9	11.8	15.5	10.1	9.83	4.36	1.00
Sc	38.3	46.0	18.2	17.8	17.1	8.58	9.42	7.76	10.9	7.29	6.24	1.94	0.10
V	217	206	159	177	119	92.7	88.0	71.9	82.5	58.8	76.8	26.0	4.47
Pb	8.38	7.75	17.1	13.7	5.64	5.75	6.78	4.24	16.0	17.5	4.28	32.0	29.2
Ga	13.9	13.4	17.7	18.6	23.0	19.2	19.8	17.5	17.1	15.6	17.8	13.8	13.2
mg#	70	69	57	55	59	52	56	49	51	50	53	35	35
Eu/Eu*	0.91	0.78	1.14	1.06	0.66	1.10	1.03	1.05	1.01	0.98	0.85	1.0	12
$(La/Yb)_N$	8.2	9.9	11.9	14.5	6.4	11.6	16	14.4	25.6	24.8	19	75	40
Sr/Y	30	23	65	55	10	38.6	48	35	67.6	88	51	120	322
Nb/Ta	17	16	19	18	18	19	19	11	30	23	10	41	5

Note. The chemical composition of the rocks corresponds to the samples 672c, 672b – gabbronorites; 672, 672a – gabbro; 696 – gabbrodiorites; 696a, 695, 696b – quartz diorites; 346, 347a, 694 – tonalites; 347, 673 – granits. Rocks in the samples 694-696 cataclazed and quartered.

This is an open access article under the CC BY 4.0 license

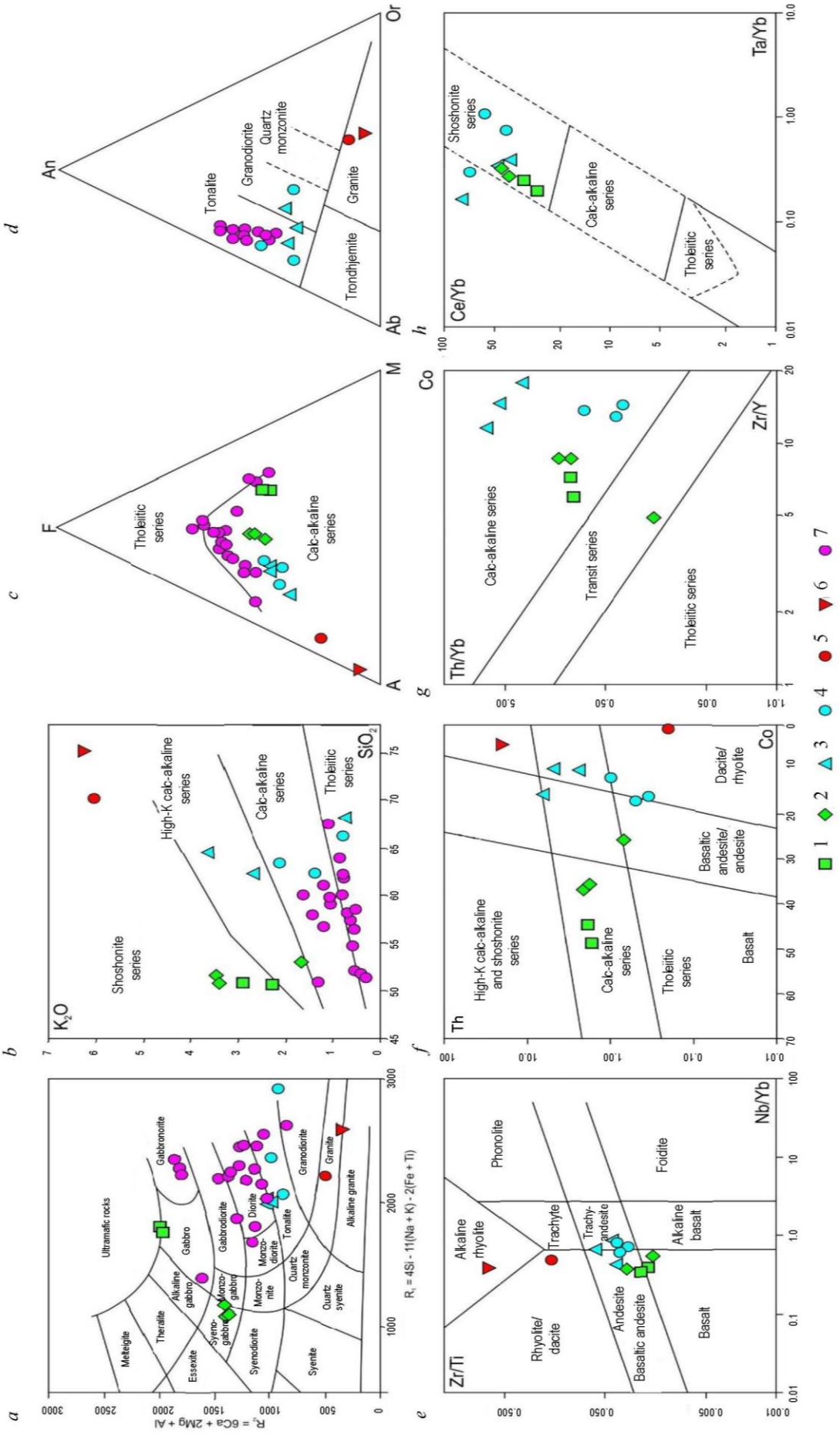


Fig.2. Geochemical diagrams for rocks of the Saltakh Massif after [21] (*a*); [22] (*b*); [23] (*c*); [18] (*d*); [20] (*e*); [17] (*f*); [24] (*g*); [20] (*h*)

1 – melanocratic two-pyroxene shists; 2 – high aluminous two-pyroxene shists; 3, 4 – Cpx-Opx plagiogneisses: 3 – quartz diorite composition, 4 – tonalite and granodiorite composition; 5 – gneissose granites; 6 – alaskitic gneissose granites; 7 – analyses of predecessors from [1] and unpublished data (A.I.Trukhalev et al., 1972)

This is an open access article under the CC BY 4.0 license

Melanocratic schists are Mg-richest (mg# = 69-70). They contain high Cr, Ni and V concentrations. The spidergrams (Fig.3, *a*, *b*) show positive anomalies for Ba, Rb, and Pb, and negative anomalies for Ta, Nb, and Zr. The rocks are enriched in REE (ΣREE = 115-130 ppm), with an indistinct Eu-minimum (Eu/Eu* = 0.78-0.91) and fractionated REE distribution $(La/Yb)_N$ = 8.2-25. In schists with more plagioclase than mafic schists, the mg# value decreases to 55-57. The spidergrams are similar, but the Ba concentration is higher (2200 ppm). The presence of a positive Sr anomaly increases Sr/Y ratio to 23-30 for melanocratic crystalline schists and 55-65 for plagiocrystalline schists. REE concentration increases (ΣREE = 162 ppm) mainly due to light lanthanides, resulting in a $(La/Yb)_N$ value of 11.9-14.5 and the formation of a positive Eu anomaly (Eu/Eu* = 1.06-1.14). Cataclased and silicified crystalline schists (sample 696) contain the highest REE concentrations (ΣREE = 286 ppm), show the Eu-minimum (Eu/Eu* = 0.66), and their REE-spectrum in the LREE field is convex.

Two-pyroxene plagiogneisses, which are petrochemically equivalent to diorites and quartz diorites, plot in the tonalite field based on their normative feldspar ratio (see Fig.2, *d*). In two cases, they are present in the granodiorite field (samples 346 and 347a, K_2O/Na_2O = 0.7-1.0). Most rocks of this group display positiveanomalies for Rb, Ba, and Pb, and negative anomalies for Ti, P, Nb, and Ta, with occasional anomalies for Th and U. The REE spidergrams are asymmetric, showing fractionated distribution in the L- and MREE fields and a flat distribution for HREE, beginning with Ho $(Ho/Yb)_N$ = 1.07-1.15. The Eu anomaly is either poorly-defined or absent (Eu/Eu* = 0.85-1.10).

Rocks with high K_2O concentrations (sample 346 and 347a) display positive anomalies for Rb, Ba, Pb, and Sr, the highest depletion in Ta and Nb, and high Sr/Y (68-88), Nb/Ta (23-30), and $(La/Yb)_N$ (248-25.6) ratios. Cataclastic varieties of two-pyroxene gneisses (samples 694 and 695) contain low concentrations of K, Cs, Rb and Ba, and elevated concentrations of U and Th. Zr/Y ratio of 5-17.8 and La/Yb ratio of 9-38 markedly exceed the indicator values for separation of tholeiitic and calc-alkaline series (> 4.5 and > 5.3, respectively) [24], indicating that the rocks discussed are part of a calc-alkaline series (Fig.2, *g*).

Granitoids are described as Mg-rich, calc-alkaline, and peraluminous (ASI = 1.12-1.14). They have potassium levels comparable to shoshonites. The trace-element and rare-earth element spectra of gneissose granites (sample 347) are similar to those of the two-pyroxene gneisses, displaying positive anomalies for Rb, Ba, Th, and Pb, and negative anomalies for Ti, Ta, Nb, and P. A high Sr/Y ratio of 120 and the highest Nb/Ta ratio of 41 were revealed. The REE spectrum is similar to that of two-pyroxene gneisses, and Eu-minimum is absent (Eu/Eu* = 1.0), but REE distribution is more fractionated $(La/Yb)_N$ = 75.

Alaskitic granites (sample 673) display positive Rb, U, Pb, Sr, and Eu anomalies, with the highest Sr/Y ratio of 322 and the lowest Nb/Ta ratio of 5. The rocks are depleted in REE (ΣREE = 14.7 ppm), and show a fractionated REE distribution with $(La/Yb)_N$ = 40. The REE spectrum in the Er-Lu zone is convex, and there is a well-defined positive Eu anomaly (Eu/Eu* = 12).

U-Pb age. Zircon age dating (Table 2) was conducted for five samples: two-pyroxene schists (samples 672 and 696), two-pyroxene plagiogneisses (samples 696a and 346), and alaskitic gneissose granites (sample 673). For sample 672, we obtained only metamorphic zircon with discordant U-Pb age values. The upper intersection of the Discordia curve from six analyses yields an age of 1991±23 Ma.

In *Opx-Cpx schists* (sample 696) of metagabbrodiorite composition, zircon occurs as grey rounded 50-100 μm long short-prismatic grains with the elongation coefficient (EC) of 1-2. The well-defined BSE image (Fig.4, *a*, *b*) shows cores portions with sectoral and oscillatory zoning, and two types of shells: thin white, light-grey, and wider dark-grey to black. The cores have median concentrations of Th at 156 ppm and U at 237 ppm, with a Th/U ratio of 0.65. Two grains with analytical points 1.1 and 6.1 show higher Y 1198-1593 ppm and ΣREE 959-1345 ppm concentrations (Table 3). The REE spectra (Fig.5, *a*) clearly show positive Ce (Ce/Ce* = 8.38-33.4) and negative Eu (Eu/Eu* = 0.38-0.80) anomalies.

This is an open access article under the CC BY 4.0 license

Results of U-Pb (SHRIMP II) zircon analyses

Analysis spots	$^{206}Pb_c$,%	U, ppm	Th, ppm	$\frac{^{232}Th}{^{238}U}$	$^{206}Pb^*$, ppm	Age $^{206}Pb/^{238}U$, Ma	Age $^{207}Pb/^{206}Pb$, Ma	*D*, %	(1) $^{238}U/^{206}Pb$	±, %	(1) $^{207}Pb^*/^{206}Pb^*$	±, %	(1) $^{207}Pb^*/^{235}U$	±, %	(1) $^{206}Pb^*/^{238}U$	±, %	Rho
Opx-Cpx shists (sample 696)																	
1.1	0.03	381	292	0.79	124	2071±17	2096±8	1	2.639	0.93	0.12982	0.44	6.783	1.0	0.3790	0.9	0.906
2.1	0.02	412	301	0.75	128	1984±16	2016±8	2	2.774	0.95	0.12410	0.45	6.167	1.0	0.3604	0.9	0.904
3.1	0.04	252	167	0.68	81.9	2066±17	2097±9	1	2.646	0.97	0.12993	0.53	6.769	1.0	0.3779	1.0	0.878
4.1	0.13	129	64	0.52	42.5	2093±19	2074±14	–1	2.606	1.10	0.12830	0.81	6.784	1.3	0.3836	1.1	0.799
5.1	0.01	183	92	0.52	59.0	2050±18	2077±11	1	2.670	1.00	0.12843	0.65	6.631	1.2	0.3745	1.0	0.841
5.2	0.10	367	80	0.22	108	1892±16	1964±9	4	2.930	0.95	0.12050	0.53	5.669	1.1	0.3412	1.0	0.874
6.1	0.03	245	170	0.72	79.3	2060±18	2066±10	0	2.656	1.00	0.12762	0.56	6.625	1.1	0.3765	1.0	0.874
6.2	0.04	584	188	0.33	179	1965±15	1973±7	0	2.806	0.91	0.12116	0.39	5.953	1.0	0.3563	0.9	0.921
7.1	0.12	119	70	0.61	39.4	2103±19	2085±14	–1	2.592	1.10	0.12900	0.81	6.864	1.4	0.3857	1.1	0.801
8.1	0.21	94	96	1.06	28.7	1959±19	1980±19	1	2.815	1.10	0.12160	1.00	5.955	1.6	0.3551	1.1	0.739
8.2	0.05	202	99	0.51	63.2	2000±18	2059±11	3	2.748	1.00	0.12719	0.63	6.380	1.2	0.3638	1.0	0.855
9.1	0.07	211	151	0.74	69.1	2081±18	2090±11	0	2.624	1.00	0.12940	0.61	6.799	1.2	0.3811	1.0	0.858
Cpx-Opx plagiogneisses (sample 696a)																	
1.1	0.05	222	143	0.67	70.8	2035±17	2112±9	4	2.693	0.96	0.13102	0.53	6.707	1.1	0.3713	1.0	0.877
2.1	0.00	163	83	0.53	52.8	2063±18	2092±11	1	2.652	0.99	0.12958	0.60	6.737	1.2	0.3771	1.0	0.856
3.1	0.01	162	100	0.64	51.1	2020±17	2094±11	4	2.718	10.0	0.12974	0.61	6.583	1.2	0.3680	10	0.853
4.1	0.13	206	126	0.63	67.6	2086±18	2095±10	0	2.617	10.0	0.12977	0.57	6.835	1.2	0.3820	10	0.867
5.1	0.09	89	30	0.35	29.7	2118±20	2083±15	–2	2.570	1.10	0.12890	0.83	6.917	1.4	0.3891	1.1	0.795
6.1	0.08	139	64	0.47	45.5	2077±23	2101±12	1	2.630	1.30	0.13019	0.71	6.820	1.5	0.3801	1.3	0.876
7.1	0.01	212	123	0.60	67.6	2032±20	2104±9	4	2.698	1.10	0.13047	0.53	6.668	1.3	0.3706	1.1	0.905
8.1	0.07	364	27	0.08	112	1980±18	1981±8	0	2.780	1.10	0.12166	0.45	6.032	1.2	0.3596	1.1	0.921
8.2	0.08	82	40	0.50	27.0	2097±22	2099±17	0	2.600	1.20	0.13000	0.98	6.890	1.6	0.3845	1.2	0.775
9.1	0.27	17	19	1.13	5.39	1986±26	1979±36	0	2.770	1.50	0.12150	2.00	6.050	2.5	0.3608	1.5	0.601
9.2	0.00	144	63	0.45	46.8	2064±19	2072±12	0	2.649	1.10	0.12809	0.69	6.666	1.3	0.3774	1.1	0.839
10.1	0.03	539	97	0.19	162	1937±16	1988±8	3	2.853	0.93	0.12218	0.46	5.905	1.0	0.3505	0.9	0.897
10.2	0.10	208	102	0.51	67.5	2064±17	2104±10	2	2.649	0.97	0.13045	0.57	6.789	1.1	0.3775	1.0	0.864

This is an open access article under the CC BY 4.0 license

Journal of Mining Institute. *2025. Vol. 272. P. 16-39*
© Nikolai I. Gusev, Lyudmila Yu. Romanova, 2024

This is an open access article under the CC BY 4.0 license

Journal of Mining Institute. 2025. Vol. 272. P. 16-39

© Nikolai I. Gusev, Lyudmila Yu. Romanova, 2024

Analysis spots	$^{206}Pb_c$, %	U, ppm	Th, ppm	$\frac{^{232}Th}{^{238}U}$	$^{206}Pb^*$, ppm	Age $^{206}Pb/^{238}U$, Ma	Age $^{207}Pb/^{206}Pb$, Ma	*D*, %	(1) $^{238}U/^{206}Pb$	±, %	(1) $^{207}Pb^*/^{206}Pb^*$	±, %	(1) $^{207}Pb^*/^{235}U$	±, %	(1) $^{206}Pb^*/^{238}U$	±, %	Rho
Cpx-Opx plagiogneisses (sample 346)																	
1.1	0.13	348	219	0.65	110	2018±16	2040±10	1	2.720	1.0	0.12583	0.59	6.378	1.1	0.3676	1.0	0.849
2.1	0.04	558	288	0.53	170	1958±18	1945±8	–1	2.818	1.1	0.11924	0.43	5.834	1.2	0.3548	1.1	0.929
3.1	0.06	362	151	0.43	114	2014±16	2019±9	0	2.726	0.9	0.12429	0.51	6.286	1.0	0.3668	0.9	0.870
4.1	0.03	326	136	0.43	105	2048±16	2027±9	–1	2.675	0.9	0.12487	0.50	6.437	1.0	0.3739	0.9	0.879
5.1	0.00	942	328	0.36	274	1879±14	2023±6	8	2.955	0.9	0.12461	0.36	5.814	0.9	0.3384	0.9	0.922
6.1	0.38	502	200	0.41	162	2052±16	2033±11	–1	2.668	0.9	0.12529	0.64	6.475	1.1	0.3748	0.9	0.811
7.1	0.06	482	315	0.68	153	2023±15	2025±9	0	2.712	0.9	0.12471	0.48	6.340	1.0	0.3687	0.9	0.877
8.1	0.04	361	160	0.46	115	2029±16	2002±9	–1	2.703	0.9	0.12313	0.50	6.281	1.0	0.3699	0.9	0.875
9.1	0.03	424	247	0.60	133	2006±16	2031±15	1	2.739	0.9	0.12510	0.83	6.298	1.2	0.3650	0.9	0.741
10.1	0.08	247	104	0.44	79.3	2043±17	2025±11	–1	2.682	1.0	0.12470	0.63	6.410	1.1	0.3728	1.0	0.832
Alaskitic gneissose granites (sample 673)																	
1.1	0.52	171	134	0.81	49.5	1861±8	1909±27	3	2.985	0.52	0.11690	1.50	5.393	1.6	0.3347	0.5	0.323
2.1	0.00	401	146	0.38	123	1969±6	1964±10	0	2.799	0.37	0.12054	0.58	5.939	0.7	0.3573	0.4	0.533
3.1	0.00	98	89	0.94	30.2	1970±11	1975±21	0	2.797	0.63	0.12120	1.20	5.976	1.4	0.3575	0.6	0.467
4.1	0.00	72	94	1.35	22.2	1968±12	1984±24	1	2.801	0.72	0.12190	1.40	5.999	1.5	0.3570	0.7	0.470
5.1	0.19	131	119	0.94	39.7	1948±9	1970±22	1	2.834	0.56	0.12090	1.30	5.882	1.4	0.3527	0.6	0.407
6.1	1.17	109	48	0.46	32.1	1884±15	1916±69	2	2.938	0.92	0.11730	3.90	5.490	4.0	0.3395	0.9	0.231
7.1	0.06	583	201	0.36	175	1935±5	1962±10	1	2.856	0.32	0.12037	0.56	5.811	0.7	0.3501	0.3	0.498
8.1	0.00	85	121	1.48	25.9	1964±12	1979±23	1	2.808	0.69	0.12160	1.30	5.970	1.5	0.3561	0.7	0.469
9.1	0.00	77	84	1.12	23.4	1939±12	1948±24	0	2.849	0.72	0.11950	1.40	5.783	1.5	0.3510	0.7	0.467
10.1	0.25	152	155	1.05	46.8	1970±9	1971±24	0	2.796	0.54	0.12100	1.40	5.965	1.5	0.3575	0.5	0.370

Note. Pb_c and Pb* are common and radiogenic Pb respectively. The calibration errors of the standard are 0.35 %. (1) is the correction on ^{204}Pb. *D* is the discordance. Rho is the correlation coefficient. The errors of individual analyses (ratios and ages) are reported on 1σ level, and the errors of the calculated age values are on 2σ level.

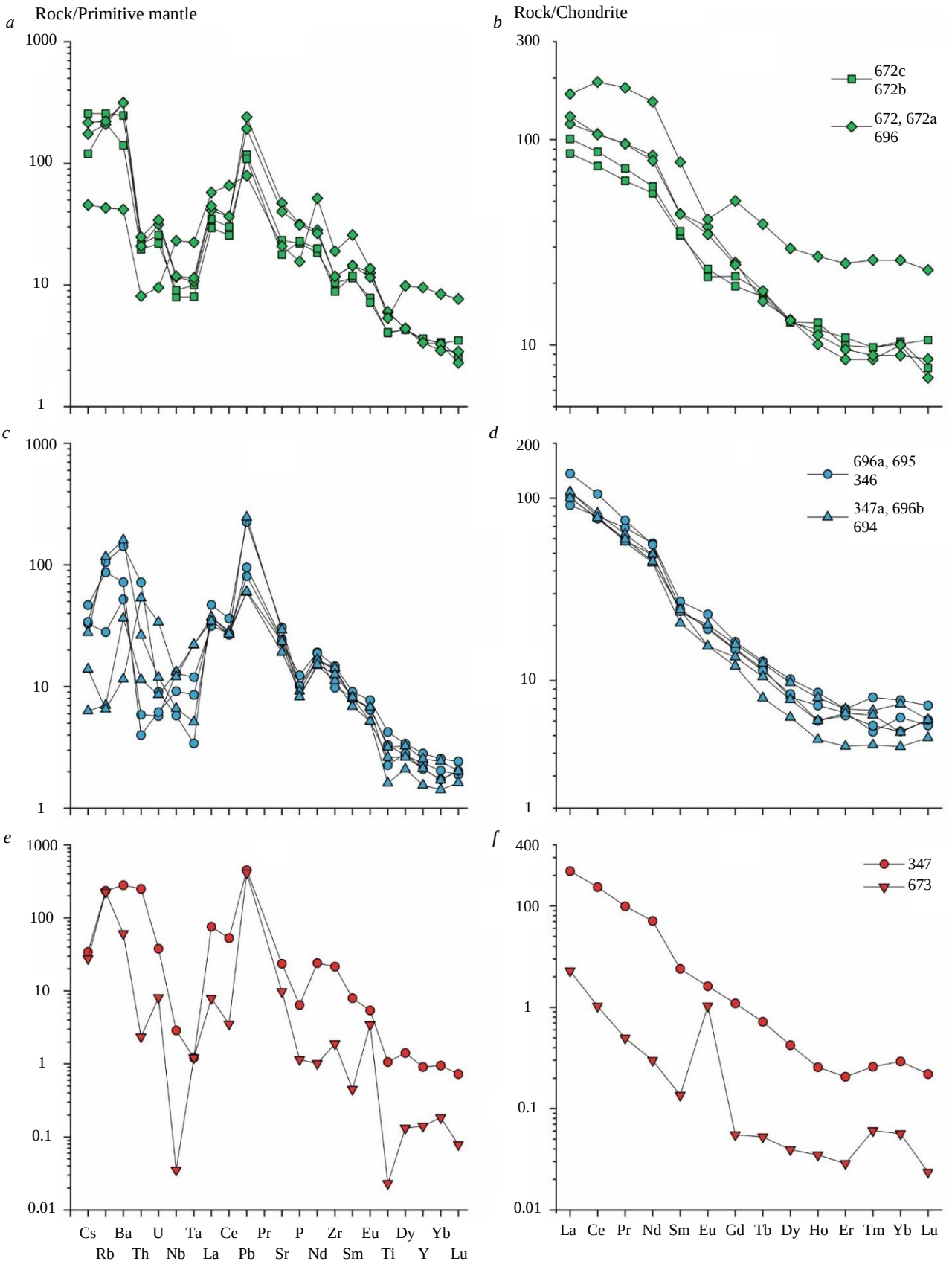


Fig.3. Multi-element diagrams for Saltakh Massif rocks: *a*, *b* – Opx-Cpx schists;
c, *d* – Cpx-Opx plagiogneisses; *e*, *f* – gneissose granites.
Concentrations were normalized for the primitive mantle and CI chondrite compositions after [25]. For sample numbers, see Table 1

This is an open access article under the CC BY 4.0 license

The REE distribution pattern is generally consistent with magmatically derived zircon, displaying a steep slope from La to Lu with positive Ce and negative Eu anomalies. In the HREE field, the spectra do not extend outside the magmatic zircon field, while the zircon is richer in LREE than a magmatic type (Fig.5, *a*). The entire zircon deviates in REE (Fig.5, *g*) from a magmatic type, occurring in the porous zircon field. U and Ca concentrations are low (Fig.5, *h*).

The shells show a lower Th/U ratio of 0.16-0.23, Th concentration of 85.2-206 ppm, U concentration of 528-917 ppm, and P concentration is lower – 108-136 ppm. Ce anomalies are weaker than those in the cores (Ce/Ce* = 4.87-7.65), but positive Eu anomalies are present (Eu/Eu* = 1.08-1.18). REE concentration in the shells are lower than in the cores (ΣREE = 164-378 ppm), and the REE distribution spectra are more subdued, showing a low $(Sm/La)_N$ ratio of 1.44-2.67. Metamorphic zircon with low Th concentration and a low Th/U ratio is crystallized near the solidus line simultaneously with monazite and allanite, which are known as major Th concentrators [26]. However, Th/U ratio decreases here due to the growth of U in zircon. P, Y, and ΣREE decrease probably due to the simultaneous zircon and apatite crystallization.

A positive Ce anomaly indicates oxidation conditions during zircon crystallization. The reduced pattern of Ce-anomaly in zircon shells indicates a decline in oxygen activity. A negative Eu anomaly in zircon cores suggests that plagioclase was crystallized together with zircon. A positive Eu anomaly in zircon shells indicates that plagioclase is dissolved, and the zircon crystallization medium is enriched in europium. Maximum age values of $^{207}Pb/^{206}Pb$ in the cores are 2103±19 Ma. The upper intersection of the Discordia line from seven measurements yields an age of 2086±8 Ma (see Fig.4, *b*). Shells that are grey in cathode luminescence (CL) contain more uranium, and show a mean Th concentration of 134 ppm, U concentration of 456 ppm, and a Th/U ratio of 0.28. A cluster of measurements made for the shells yields the value 1971±10 as the upper intersection of the Discordia line from three measurements, indicating multiple partial melting processes. Thin white shells have not been studied due to their thinness.

Cpx-Opx plagiogneisses (sample 696a), petrochemically equivalent to quartz metadiorites, contain zircon similar to sample 696 (Fig.4, *c*, *d*). Shells that are white in CL are wider and can thus be dated. The cores of grains displays the following mean concentrations, ppm: Th 134, U 317, Th/U 0.40, Y 624, Nb 25; ΣREE = 524. The increase in REE concentration is accompanied by a decrease of the Eu-minimum. The Eu/Eu* ratio is generally 0.33-0.66, while at points 1.1 and 4.1, where ΣREE increase to 564-598 ppm, the Eu-anomaly increases and becomes positive (Eu/Eu* = 1.03-2.89). Zircon cores, like those in sample 696, are enriched in LREE (Fig.5, *b*), but some of the cores are enriched in Ca (Fig.5, *h*). The Discordia line, constructed from nine measurements in zircon cores, yields an upper intersection at 2100±7 Ma (Fig.4, *d*), which is accepted as the time of zircon crystallization in the magmatic protolith of two-pyroxene plagiogneisses.

The shell, which is white in CL, with the analytical point 9.1, shows an age of 1986±26 Ma and low Th (24) and U (48) concentrations (ppm), but a Th/U ratio of 0.51 is similar to that of magmatic zircon. Negative Eu anomaly (Eu/Eu* = 0.65) and positive Ce anomaly (Ce/Ce* = 19.8) are well-defined. At this point, REE concentration is lower than in the cores (Fig.5, *c*), and the Eu-minimum decreases (Eu/Eu* = 0.65). Later shells that are dark in CL (points 8.1 and 10.1) show higher concentrations than in white shells, ppm: Th 56-100, U 701-786, and a low Th/U ratio of 0.08-0.13 typical of metamorphic zircon. They generally show low REE (ΣREE = 192-239 ppm), Y of 156-238 ppm, and Ce/Ce* of 3.22-3.58, but they are enriched in Eu (Eu/Eu* = 1.54-2.92), Li 9.72-11.36 ppm, and Hf 15124 ppm. The Discordia line from three measurements in metamorphic shells yields an upper intersection with an age of 1984±11 Ma indicating the time of metamorphism.

Cpx-Opx plagiogneisses (sample 346), petrochemically equivalent to metatonalites, contain grey zircon crystals with yellow and pink shades of colour. These semi-transparent, subidiomorphic crystals exhibit thin, well-defined growth zones under an optical microscope (Fig.4, *e*, *f*). The crystals are 100-220 μm long, with their EC of 2-4. The zircons are dark in CI and their zoning is either oscillatory or is present as relics.

This is an open access article under the CC BY 4.0 license

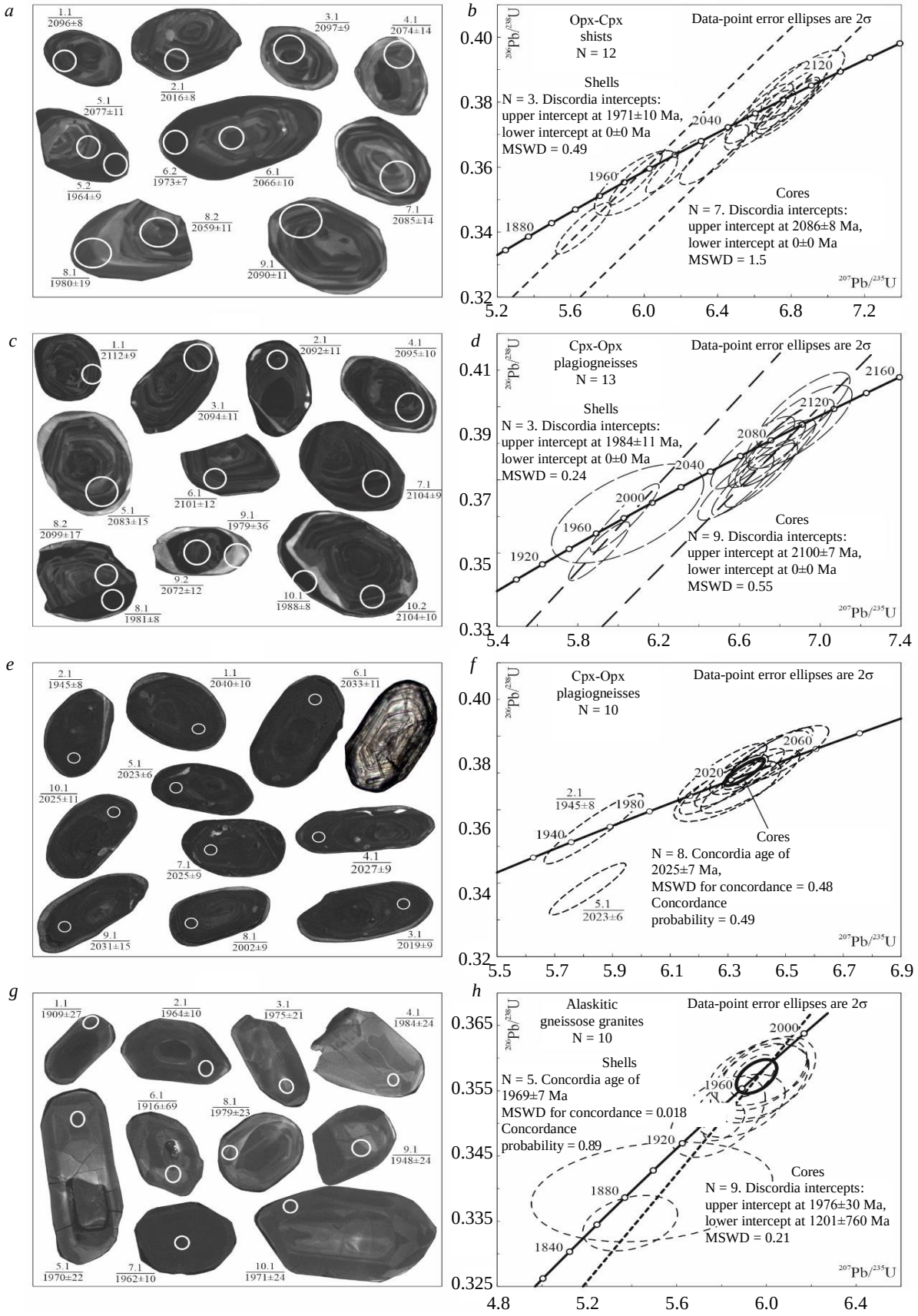


Fig.4. Cathode luminescent images and age of zircon from Opx-Cpx schists (sample 696) (*a*, *b*); Cpx-Opx plagiogneisses (sample 696a) (*c*, *d*); Cpx-Opx plagiogneisses (sample 346) (*e*, *f*); alaskitic gneissose granites (sample 673) (*g*, *h*). From here onwards, white circles indicate analytic craters. Analysis number is in the numerator and $^{207}Pb/^{206}Pb$ age is in the denominator. The crater is about 20 μm in diameter

This is an open access article under the CC BY 4.0 license

This is an open access article under the CC BY 4.0 license

Table 3

Concentrations (ppm) of trace elements and REE in the zircon

Element	Opx-Cpx shists (sample 696)									Cpx-Opx plagiogneisses (sample 696a)									
	1.1	3.1	4.1	5.1	5.2	6.1	6.2	7.1	9.1	1.1	2.1	3.1	4.1	5.1	6.1	7.1	8.1	8.2	9.1
La	2.06	0.31	0.13	1.28	0.73	1.08	2.75	0.64	0.30	2.04	0.06	0.35	0.62	1.36	0.50	0.35	1.60	1.61	0.30
Ce	67.7	27.1	21.8	27.4	17.8	38.3	36.4	27.8	34.2	39.6	25.4	27.5	31.4	15.8	21.2	31.4	16.4	31.4	25.1
Pr	1.53	0.36	0.19	0.49	0.43	1.11	1.19	0.58	0.31	1.64	0.12	0.43	1.23	0.43	0.58	0.27	0.77	0.89	0.31
Nd	11.3	2.20	1.63	2.32	2.42	8.11	5.95	3.52	2.77	10.3	1.24	3.16	9.94	2.01	4.40	2.97	3.95	6.04	1.42
Sm	10.8	3.16	2.58	1.96	1.23	8.30	2.47	3.03	2.90	4.90	2.07	2.64	5.35	1.03	2.99	3.08	1.22	6.22	1.24
Eu	3.92	0.91	0.63	1.11	0.66	2.40	1.64	0.79	0.86	8.11	0.52	0.56	3.01	0.25	1.36	1.22	1.83	2.47	0.63
Gd	43.3	14.3	9.93	9.05	2.83	32.7	7.28	10.0	14.3	15.0	9.00	9.83	14.7	3.76	12.0	12.4	3.02	23.4	6.98
Dy	140	61.5	46.7	36.0	12.2	102	29.8	35.3	55.5	54.2	38.8	35.6	53.8	14.6	48.8	48.0	12.0	72.4	28.3
Er	299	149	110	86.7	29.4	216	70.6	82.9	125	125	91.6	86.6	120	37.6	123	119	35.0	157	63.8
Yb	651	370	267	205	80.4	467	185	184	284	285	218	199	273	97.6	291	262	97.0	325	138
Lu	115	69.5	47.0	37.2	15.9	81.9	34.7	34.0	51.0	52.8	42.2	36.0	50.4	18.2	57.2	47.2	19.4	57.1	24.9
Li	3.61	5.08	2.94	6.85	12.9	1.19	13.5	2.99	7.58	5.53	3.07	7.10	5.01	2.58	3.98	6.57	9.72	2.46	1.96
P	220	275	158	292	136	175	108	88.4	158	139	118	111	177	208	207	165	66.9	93.8	188
Ca	10.7	31.5	6.74	34.6	123	11.1	6.42	4.36	10.0	173	2.27	27.5	27.3	191	29.8	2.77	4.03	7.13	52.5
Ti	13.6	6.75	8.98	10.9	9.79	7.48	10.8	16.0	7.25	35.5	8.00	13.8	8.88	5.91	9.08	7.16	6.88	7.55	8.51
Sr	0.67	0.46	0.50	0.65	0.83	0.62	0.39	0.45	0.65	2.29	0.34	0.66	0.81	0.77	1.20	0.51	0.57	0.55	0.72
Y	1593	806	576	480	170	1198	402	444	710	711	506	521	679	203	650	621	156	859	315
Nb	83.4	60.9	50.0	61.6	46.9	29.9	34.9	35.7	36.4	29.3	36.4	22.3	20.4	24.1	12.4	20.6	12.4	27.5	30.1
Ba	1.46	1.10	2.15	2.58	3.60	1.98	2.06	2.49	2.21	10.2	1.72	2.73	1.47	1.14	1.83	1.71	1.29	1.03	3.18
Hf	13762	10718	10525	11602	9958	11246	12595	11482	10775	8544	11389	11819	11338	12507	12034	12266	15124	13708	13436
Th	418	171	65.7	153	85.2	217	206	85.0	354	154	104	137	161	34.6	85.3	306	56.2	95.4	24.3
U	708	384	192	392	528	418	917	200	523	300	271	289	345	133	264	488	701	375	48
Th/U	0.59	0.44	0.34	0.39	0.16	0.52	0.23	0.42	0.68	0.51	0.38	0.47	0.47	0.26	0.32	0.63	0.08	0.25	0.51
Eu/Eu*	0.55	0.41	0.38	0.80	1.08	0.44	1.18	0.44	0.40	2.89	0.37	0.33	1.03	0.39	0.69	0.60	2.92	0.62	0.65
Ce/Ce*	9.23	19.7	33.4	8.38	7.65	8.49	4.87	11.0	27.0	5.23	72.7	17.1	8.71	5.02	9.55	24.7	3.58	6.36	19.8
ΣREE	1345	699	507	408	164	959	378	383	571	598	429	401	564	193	563	528	192	684	291
ΣLREE	82.6	30.0	23.7	31.4	21.4	48.6	46.3	32.6	37.6	53.5	26.8	31.5	43.2	19.6	26.7	35.0	22.7	39.9	27.1
ΣHREE	1248	665	480	374	141	900	327	346	530	532	400	367	512	172	532	489	166	635	262
$(Lu/La)_N$	538	2148	3450	281	209	734	122	509	1643	249	6551	989	781	129	1097	1316	116	343	804
$(Lu/Gd)_N$	21.5	39.4	38.3	33.3	45.6	20.3	38.6	27.4	28.9	28.5	37.9	29.6	27.7	39.1	38.7	30.7	51.9	19.8	28.8
$(Sm/La)_N$	8.41	16.2	31.5	2.46	2.67	12.4	1.44	7.55	15.5	3.85	53.5	12.1	13.8	1.21	9.53	14.3	1.21	6.19	6.65
T(Ti),°C	771	710	734	751	741	718	750	786	715	869	724	772	733	699	735	714	711	719	729

Element	Cpx-Opx plagiogneisses (sample 696a)			Cpx-Opx plagiogneisses (sample 346)								
	9.2	10.1	10.2	1.1	3.1	4.1	5.1	6.1	7.1	8.1	9.1	10.1
La	2.42	2.03	0.64	10.4	5.58	6.64	22.7	7.59	7.07	2.89	28.7	14.0
Ce	35.6	15.5	37.4	88.4	56.9	65.4	106	80.7	49.1	38.9	301	87.1
Pr	2.13	0.67	0.41	10.2	5.83	4.44	14.0	6.28	3.48	2.54	31.4	17.8
Nd	14.6	3.15	3.13	76.1	43.7	30.8	65.8	46.8	23.9	16.5	198	130
Sm	4.87	1.15	3.75	28.0	12.3	12.2	11.6	14.7	9.38	8.67	32.4	24.2
Eu	1.52	1.05	1.14	5.23	2.67	1.82	4.07	3.47	2.62	1.45	16.6	7.00
Gd	11.6	3.73	16.2	48.8	17.9	20.8	29.4	21.9	22.0	16.8	41.8	42.2
Dy	35.6	17.0	75.4	85.9	40.6	39.3	82.2	33.2	54.7	31.3	40.7	55.9
Er	96.1	45.3	205	169	79.8	88.3	200	71.1	128	78.5	115	109
Yb	238	124	472	381	206	224	580	168	304	196	306	267
Lu	43.9	24.6	93.1	69.5	40.9	41.6	126	32.9	55.3	33.8	51.4	54.0
Li	4.14	11.4	2.61	2.55	9.32	6.12	27.5	9.51	2.98	5.28	6.07	9.78
P	913	66.0	268	96	185	135	205	15	61	164	97	124
Ca	1273	20.4	61.2	99	76	82	3558	240	96	122	220	577
Ti	8.38	8.74	10.0	19.5	15.7	12.0	28.6	10.8	12.2	9.97	22.5	24.5
Sr	3.46	0.63	0.65	1.80	1.09	1.33	123	5.01	3.43	2.37	7.17	2.90
Y	476	236	1018	937	500	487	1 198	333	711	421	482	702
Nb	33.8	18.6	25.1	100	63.1	54.9	35.8	56.2	48.8	42.0	81.0	64.9
Ba	2.90	2.05	1.56	3.28	2.59	1.54	11.8	8.23	6.64	6.27	11.7	9.56
Hf	12532	13032	11668	13227	15900	12755	19615	14366	11381	10908	12556	15979
Th	86.4	100	176	284	225	186	494	262	265	149	312	189
U	252	786	453	613	687	567	2 903	709	564	453	713	589
Th/U	0.34	0.13	0.39	0.46	0.33	0.33	0.17	0.37	0.47	0.33	0.44	0.32
Eu/Eu*	0.61	1.54	0.44	0.43	0.55	0.35	0.67	0.59	0.56	0.37	1.37	0.67
Ce/Ce*	3.79	3.22	17.7	2.08	2.41	2.91	1.43	2.83	2.39	3.48	2.42	1.33
ΣREE	487	239	909	972	512	535	1241	486	660	428	1162	809
ΣLREE	54.7	21.4	41.5	185	112	107	208	141	84	61	558	249
ΣHREE	425	215	862	754	385	414	1017	327	564	357	555	529
$(Lu/La)_N$	175	117	1408	64.4	70.6	60.3	53.2	41.8	75.3	113	17.2	37.1
$(Lu/Gd)_N$	30.5	53.3	46.4	11.5	18.5	16.2	34.6	12.2	20.4	16.3	9.90	10.4
$(Sm/La)_N$	3.22	0.91	9.42	4.31	3.52	2.93	0.82	3.09	2.12	4.81	1.81	2.76
T(Ti),°C	728	731	743	805	785	759	845	750	761	743	820	829

Note. Analytical spot numbers correspond to those in Fig.4; *T*(Ti),°C is the zircon crystallization temperature evaluated by the thermometer [27].

This is an open access article under the CC BY 4.0 license

Journal of Mining Institute. 2025. Vol. 272. P. 16-39
© Nikolai I. Gusev, Lyudmila Yu. Romanova, 2024

Journal of Mining Institute. 2025. Vol. 272. P. 16-39
© Nikolai I. Gusev, Lyudmila Yu. Romanova, 2024

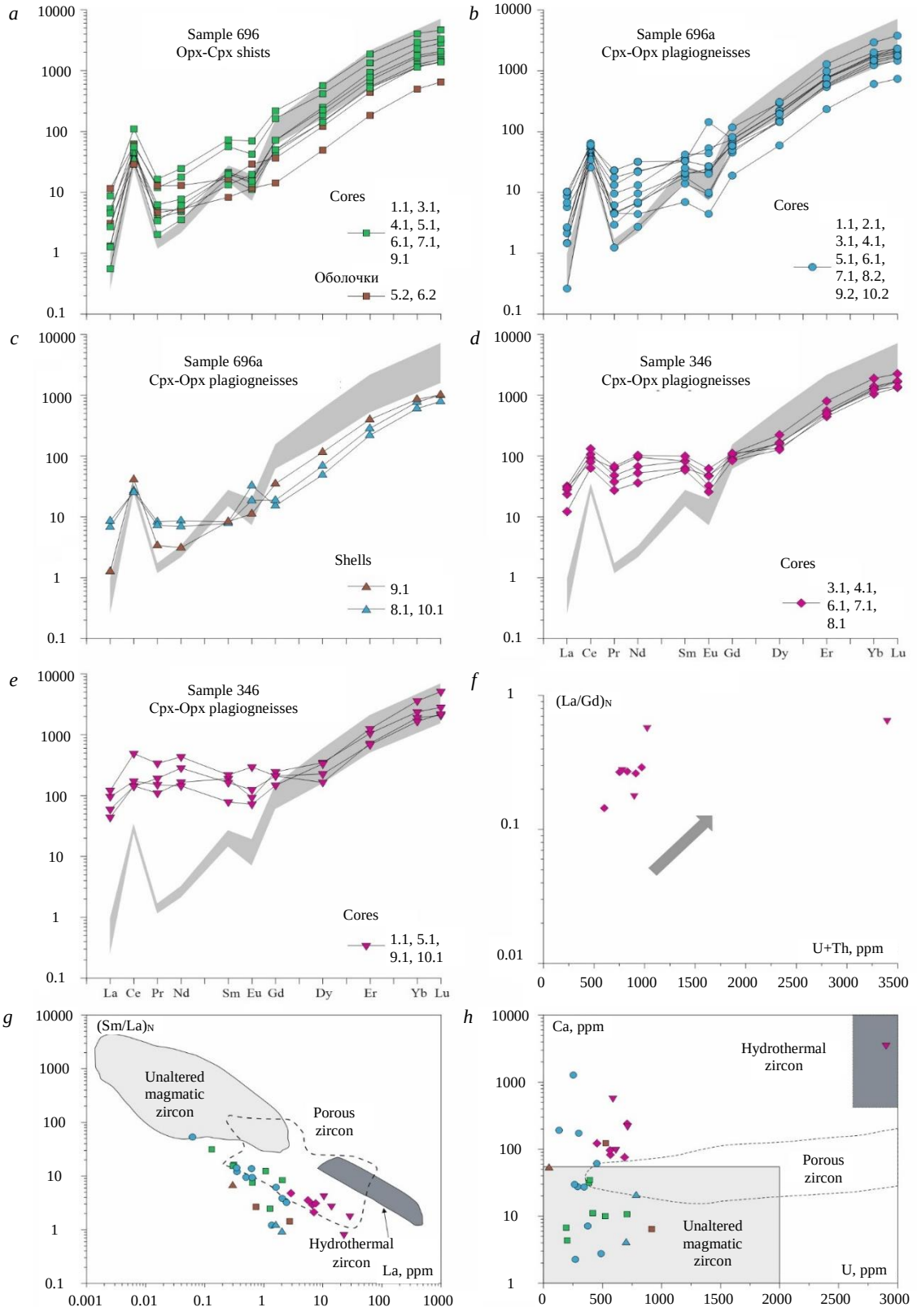


Fig.5. Geochemical diagrams for zircon from Saltakh rocks: *a-e* – diagrams showing REE distribution in zircon from samples 696, 696a and 346. Concentrations normalized for CI chondrite composition after [25]. Grey field – magmatic zircon composition after [28]. Numbers of spectra are consistent with the numbers of analytical points in Fig.4 and in Table 2; *f* – types of zircon in $(La/Gd)_N$-U+Th diagrams (after [29], arrow indicates a LREE concentration trend, provoked by the damage of the crystalline lattice due to radioactive irradiation); *g*, *h* – $(Sm/La)_N$-La and Ca-U diagrams after [30]. Porous zircon is understood as altered magmatic zircon produced by dissolution-redeposition in the presence of water fluid [31]

This is an open access article under the CC BY 4.0 license

The zircons contain, ppm: Th 149-494, U 453-713, and Th/U 0.17-0.46. Their distinctive feature is LREE concentration (Fig.5, *d*, *f*). Their REE-richest spectra (ΣLREE = 185-558 ppm) are shown in Fig.5, e. Based on its LREE enrichment, the mineral falls within the porous zircon field, (Fig.5, *g*). Ca concentration is also high (Fig.5, *h*). The zircons exhibit a poorly defined positive Ce anomaly (Ce/Ce* = 1.33-2.91) and and a poorly defined Eu-minimum (Eu/Eu* = 0.35-0.67). The Eu/Eu* ratio shows a positive value (1.37) in zircon with point 9.1. Characteristic Hf concentrations range from 10908 to 19615 ppm.

Most of the figurative points of zircon form a compact field on the Concordia line. A concordant age of 2025±7 Ma was obtained for eight points (see Fig.4, *e*, *f*), except for a grain with an analysis 5.1 showing 8 % discordance and a grain at 2.1, with an age of 1945±8 Ma. The discordant grain with analysis 5.1 contains anomalously high Ca, Sr, P, Y, REE, Th, U, and Hf concentrations.

Zircon from sample 346 has a low $(Lu/Gd)_N$ value of 16.3-34.6. In LREE-richest grains (analytical points 1.1, 6.1, 9.1 and 10.1) a low $(Lu/Gd)_N$ value of 9.9-12.2 suggests the presence of garnet in paragenesis during zircon crystallization.

Zircon from the *alaskitic gneissose granites* (sample 673) appears as grey transparent and semi-transparent, prismatic, and rounded idiomorphic to subidiomorphic crystals. The crystals are 200-400 μm in length with an EC of 1-2. Zircon grains in CL are polygenic, with occasionally identifiable cores and shells. Many grains exhibit coarse concentric and mottled zoning. Zones that are light in CL contain 97 ppm of Th and 83 ppm of U, with a Th/U ratio of 1.22. The grain margins are generally black in CL, containing higher Th (258 ppm) and U (134 ppm) concentrations and have a Th/U ratio of 0.67. The Discordia line from 10 analyses yields an upper intersection age of 1969±7 Ma, which coincides with the age 1971±10 Ma of black shells in sample 696, suggesting the age of rock anatexis in the Saltakh zone and the crystallization age of alaskitic anatectic melt.

The isotopic Sm-Nd and Rb-Sr systems of the analyzed rocks were studied in five samples (Table 4). In most rocks, $^{147}Sm/^{144}Nd$ ratios vary slightly (0.10-0.11), generally lower than a medium crustal value (0.12). All the rocks have positive $\varepsilon_{Nd}(T)$ values ranging from +1.9 to +4.1. Their points are plotted just below the Nd evolution line in a depleted mantle source (Fig.6, *a*), indicating a magma source had a very short crustal prehistory. Only the gabbroic rocks of sample 696 align with the mantle sequence of rock evolution (Fig.6, *b*). The other rocks deviate due to enrichment in radiogenic strontium. Schists in sample 672c exhibit anomalous Nd isotopic characteristics, likely due to multiple processes.

Table 4

Nd and Sr isotope composition on the rocks of the Saltakh Massif

Sample	Age, Ma	Sm, ppm	Nd, ppm	$^{147}Sm/^{144}Nd$	$^{143}Nd/^{144}Nd$	$\varepsilon_{Nd}(T)$	$T_{(Nd)}$DM, Ga	Rb, ppm	Sr, ppm	$^{87}Rb/^{86}Sr$	$^{87}Sr/^{86}Sr$	$\varepsilon_{Sr}(T)$
346	2025	3.94	24.9	0.0957	0.511397	2.1	2.26	65.9	727	0.2621	0.710767	12.0
672	2100	6.79	37.8	0.1085	0.511515	1.9	2.36	133	1116	0.3454	0.713067	8.37
672c	2100	4.49	18.5	0.1469	0.512868	18	–	148	526	0.8136	0.728116	21.0
696	2100	13.9	73.6	0.1144	0.511683	3.6	2.25	29.5	512	0.1667	0.707128	0.77
696a	2100	4.96	27.7	0.1082	0.511621	4.1	2.20	18.6	545	0.0986	0.706265	17.8

Discussion

The Saltakh Massif consists of granulite-facies two-pyroxene schists and plagiogneisses. A differentiated series of rocks, ranging from gabbro to tonalities, was reconstructed, based on their chemical composition. Despite granulite-facies metamorphism, Saltakh rocks have many features indicative of a shoshonitic type. It has been noted in [32] that shoshonitic series have a high K_2O/Na_2O ratio > 0.5, normative hypersthene ± olivine, low iron, high LILE, high but variable Al_2O_3 (9-20 wt.%) and

This is an open access article under the CC BY 4.0 license

Journal of Mining Institute. 2025. Vol. 272. P. 16-39
© Nikolai I. Gusev, Lyudmila Yu. Romanova, 2024

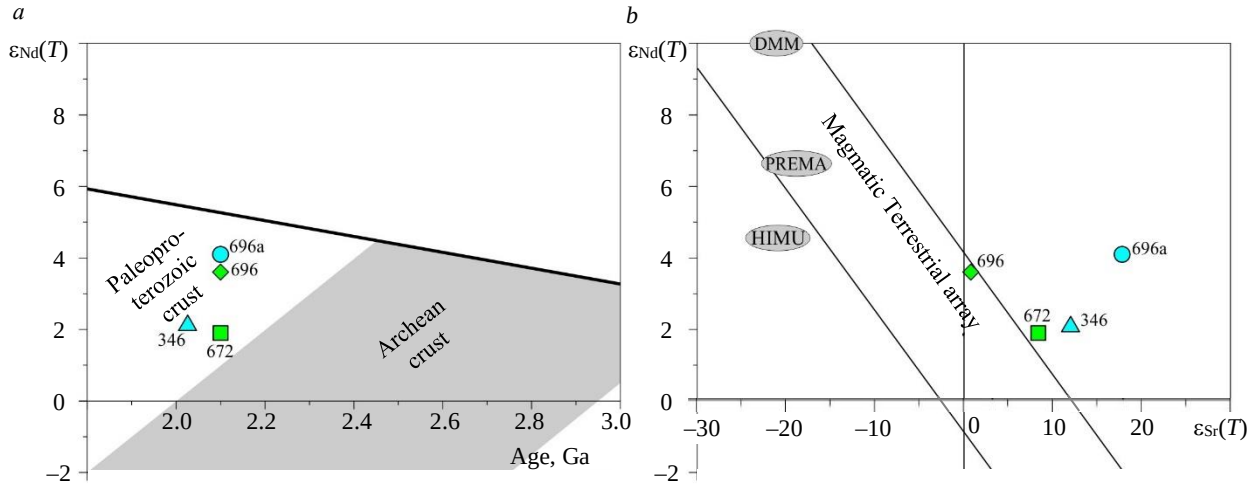


Fig.6. Diagrams of $\varepsilon_{Nd}(T)$ – age (*a*) and $\varepsilon_{Nd}(T)$ – $\varepsilon_{Sr}(T)$ (*b*) for Saltakh Massif rocks. DMM, PREMA, HIMU reservoirs were normalized for their modern isotopic parameters after [33]. Primary isotopic ratios and $\varepsilon_{Nd}(T)$ and $\varepsilon_{Sr}(T)$ values were calculated using values for CHUR $^{143}Nd/^{144}Nd = 0.512638$, $^{147}Sm/^{144}Nd = 0.1967$; UR $^{87}Sr/^{86}Sr = 0.7045$, $^{87}Rb/^{86}Sr = 0.0827$

low TiO_2 concentration. Shoshonites are enriched in both alkaline and alkaline-earth elements, as well as in P, Ce, and Sm, while the concentrations of other incompatible elements, such as Ta, Nb, Zr, Hf, Ti, Y and Yb, remain low [20]. In spite of the slight prevalence of K over Na in some rocks, it is elevated Ce and low Yb concentrations that were responsible for the presence of Saltakh rocks in the shoshonite field (see Fig.2, *h*).

Saltakh rocks are rich in magnesium: mg# is 55-70 in two-pyroxene schists and 50-56 in two-pyroxene plagiogneisses. The protoliths of mafic granulites display the cumulative accumulation of plagioclase. Hence, Al_2O_3, Sr, Ba and REE concentrations increase and positive Eu anomaly appears. Geochemical features ([34] such as MgO/FeOt < 1.39; TiO_2 < 0.41 wt.%; Yb < 1.36 ppm; Sc 38-46 ppm; Eu/Eu* = 0.78-0.91), indicate that the protoliths of melanoschists are non-cumulative rocks, while those of leucoschists (Sc < 33 ppm; Eu/Eu* = 1.06-1.14) are intermediate between cumulative and non-cumulative gabbroic rocks.

Plagiogneisses of diorite composition contain lower Yb (1.02-1.26 ppm), and have more fractionated REE $(La/Yb)_N$ = 11-16. As their silicic acid content increases, Y decreases from 16.5 to 9.55 ppm and the Sr/Y ratio increases to 35-48. The elevated Sr/Y ratio (> 20) is attributed to an abundance of water in the melt, which contributes to the crystallization and fractionation of a phenocryst phase (amphibole and/or biotite), while suppressing plagioclase crystallization [35]. This process is most distinct in two-pyroxene gneisses of tonalite composition (samples 346 and 347a), Sr/Y = 67.6-88. Tonalites are more depleted in HREE $(La/Yb)_N$ = 24.8-25.6, likely due to garnet fractionation. The presence of garnet in the restite is supported by trace element concentrations in zircon, with a low $(Lu/Gd)_N$ value (zircon of sample 346, $(Lu/Gd)_N$ = 9.9-12.2) indicating the presence of garnet in paragenesis upon zircon crystallization. Garnet fractionation is indicated by the increase in $(Dy/Yb)_N$ [36] zircon in mafic rocks $(Dy/Yb)_N$ = 1.23-1.26 to 1.43-1.58 in felsic varieties.

The geochemical characteristics of tonalites suggest that the melt was formed at depth in equilibrium with a garnet-bearing association. Garnetiferous rock varieties are fractionated under similar high-pressure conditions in an aquatic medium, resulting in the formation of TTG-rocks in the lower zone of the island-arc crust [37].

This is an open access article under the CC BY 4.0 license

Differences in the geochemistry of potassium granites are noteworthy (see Fig.3, *e*, *f*). Gneissose granites (sample 347) form bands within tonalites. They differ in REE distribution from the 1967±7 Ma anatectic gneissose granites of sample 673 but are similar to tonalites of samples 346 and 347a dated at 2025±7 Ma. Their trace and rare-earth distribution spectra are conformal, showing slightly higher concentrations of Rb, Ba, Th, Pb, Zr, and LREE, but with better-defined depletions in Ti, Ta, Nb, P, and HREE. It appears that the granites of sample 347 were produced by a 2025±7 Ma old impulse of magmatism.

The age of the Saltakh Massif. Zircon monofractions from metadiorites in the northern zone of the massif were dated – the results showed a U-Pb age of 2100-2086 Ma. The structure and geochemistry of the dated zircon cores indicate its magmatic origin. In sample 696, a maximum age value in the cores is 2103±19 Ma, while an age of 2086±8 Ma was obtained from an upper intersection of the Discordia line. For highly metamorphosed rocks, the age decrease along the Concordia line could be due to the loss of radiogenic lead induced by prolonged impact of granulite-facies metamorphism [38]. Thus, an age date of approximately 2100 Ma is the most reliable estimate for the crystallization age of Saltakh gabbrodiorites and diorites.

A smaller concordant age of 2025±7 Ma was obtained for zircon from metatonalites (sample 346) in the southeastern portion of the massif. In CL, these zircons appear magmatic, but their geochemistry differs from that of magmatic zircon due to enrichment in LREE. This type of enrichment has been previously reported for porous zircon described as microporous zircon with hydrothermally indicative geochemistry. Despite this, their morphology does not differ from that of magmatic zircon magmatic zircon [31].

The main characteristic of "typical" REE distribution in magmatic zircon is the increase in REE concentration from La to Lu, as the compatibility of REE with smaller ionic radii increases in this direction in zircon at $La_N > 10$. Th zircon composition (see Fig.5, *g*) closely resembles the porous zircon field, but in Fig.5, *h*, the LRRE-enriched analyses are in the uncertainty field. The anomalous LREE enrichment in zircon could also be due to disequilibrated REE distribution between the rock and the melt, defects imperfections in zircon's crystalline lattice, radioactive U and Th decay damaging zircon's crystalline lattice and multiple hydrothermal processes [39-41].

Elevated LREE concentrations, caused by the presence of monazite or orthite aggregates in zircon fractures, are generally accompanied by an increase in Th [42]. However, in zircon from sample 346, U and Th concentrations are low, and Th does not correlate with LREE (Fig.5, *f*). If inclusions were formed in fractures, then high- and low-LREE zircon analyses could be expected, but all the analyzed zircon from sample 346 is enriched in LREE.

The damage of zircon's crystalline lattice by radioactive U and Th decay is conducive to its LREE enrichment affected by hydrothermal fluids [39] that induce cation exchange in the crystalline lattice. Such enrichment is indicated by a positive correlation between U+Th and the increase of LRRE indicated by a (La/Gd)N ratio [29]. As no correlation of this type has been revealed (Fig.5, *f*), LREE enrichment is not related to radioactive irradiation.

The effect of fluid is felt in zircon with analytical crater 5.1, where the U-Pb isotope system is distorted (discordance $D = 8$ %), and non-formula element concentrations (Ca, Sr, P, Y, REE, Th, U and Hf) in zircon are anomalously high [43]. In Fig.5, *h*, the grain is in the hydrothermal zircon field. In other cases, the U-Pb system discordance is low, and non-formula element concentrations do not differ markedly from those of zircon with a typical magmatic profile on other spidergrams, except for the Ca enrichment of high-LREE zircon that is shown in Fig.5, *h*.

A quantitative assessment of the chemical alterations in zircon (LREE-I index after [44] LREE-I = (Dy/Nd) + (Dy/Sm)) indicates that all of the zircon samples are altered LREE-I = 1.5-8.3 (for altered zircon, this value is expected to be < 10).

This is an open access article under the CC BY 4.0 license

LREE enrichment, along with the disturbance of estimated zircon/melt distribution coefficients, has been observed in zircon from sanukitoids. This is due to the originally imperfect structure of the mineral formed upon the crystallization of zircon from melt at high temperature in an anomalous fluid regime [6, 30, 45]. Both Saltakh rocks and sanukitoids [46-48] belong to the shoshonite series or are related to it for tonalities in sample 346. This suggests high temperature crystallization and an anomalous fluid regime leading to the LREE enrichment of zircon. LREE enrichment could have been induced by the simultaneous crystallization of hornblende and clinopyroxene, which remove MREE and HREE from the melt, causing the LREE oversaturation of the melt [29].

We interpret concordant U-Pb age of 2025±7 Ma obtained for porous zircon not as a sign of rejuvenation provoked by hydrothermal alterations, but rather as indicative of the disturbance of the U-Pb isotope system. Most of the age values obtained are concordant. In addition, similar isotopic dating results for metamagmatic rocks have been obtained in the Khapchan belt, located 170 km south of the Saltakh Massif, in the Khapchan prospect, where the concordant U-Pb age of zircon from the dioritic protolith of two-pyroxene plagioschists is 2095±10 Ma, while the tonalitic protolith of two-pyroxene plagiogneisses is 2030±17 Ma. Hence, the Saltakh Massif should be described as polychromous, containing gabbro and diorites dated at ca. 2100 Ma and younger tonalites dated at 2025 Ma.

Geodynamic setting. Calc-alkaline and shoshonitic magmatism is typomorphic for active continental margins. Shoshonitic magmatism in subduction orogens is generally simultaneous with or takes place after calc-alkaline magmatism during postorogenic extension [49, 50]. Experiments have demonstrated that the high-pressure fractional crystallization (10 kbar) of calc-alkaline magma resulting in shoshonite formation, may take place at the base of thick crust in continental or highly mature arcs [51]. The origin of shoshonitic magmatism is related to thermal events in the mantle generally caused by slab detachment or underplating, which can be brought about by the intrusion of basaltic magma into the lower portion of the crust upon extension [49]. Shoshonitic series are known in continental, oceanic, and postcollisional magmatic arc settings, and in intraplate settings [19, 20].

According to the algorithm for assessing the geodynamic setting for rocks of potassium alkalinity ([19], the sequence of diagrams in Fig.7, *a*-*d*), Saltakh rocks do not fit the profile of intraplate magmatic products (Fig.7, *a*, *b*). In Fig.7, *c*, *d*, they are classified as potassium magmatic products (derived from shoshonitic magma) of continental arcs. It should be noted that metagabbroic rocks are consistent with postcollisional arc rocks. A similar geodynamic setting is reconstructed using other poorly mobile elements, e.g., Nb, La, Th and Yb (Fig.7, *e*, *f*).

The compositions of Saltakh rocks are plotted in the alkaline arc field (Fig.7, *e*). The position of gabbroic rocks in the oceanic island field in Fig.7, *f* is likely due to the Th depletion of gabbroic rocks during granulite-facies metamorphism. According to the authors of diagrams 7, *e*, *f* [34], the Aeolian [52] and Apennine-Magrib arcs in the modern Western Mediterranean region [53], related to the postorogenic extension of the Earth's crust, are the tectonotype of modern alkaline arcs.

Available geochemical data indicate that the Saltakh zircon was formed in the continental crust and was concentrated in the continental arc field (Fig.7, *g*). The upward elongation of the point field is interpreted as the formation of magma from an enriched mantle source or the addition of crustal material to the mantle source. In Fig.7, *h*, the zircon composition is positioned in the mantle rock sequence, primarily due to low Yb concentration in zircon, supported by positive $\varepsilon_{Nd}(T)$ values ranging from +1.9 to +4.1 for Saltakh Pluton rocks.

Thus, the geodynamic setting in which the Saltakh Massif was formed appears to be consistent with a near-continental magmatic arc, which experienced postorogenic extension. Shoshonitic series are generally formed in post-collisional, intra-arc, and back-arc rifts, when a compression setting is followed by an extension regime.

This is an open access article under the CC BY 4.0 license

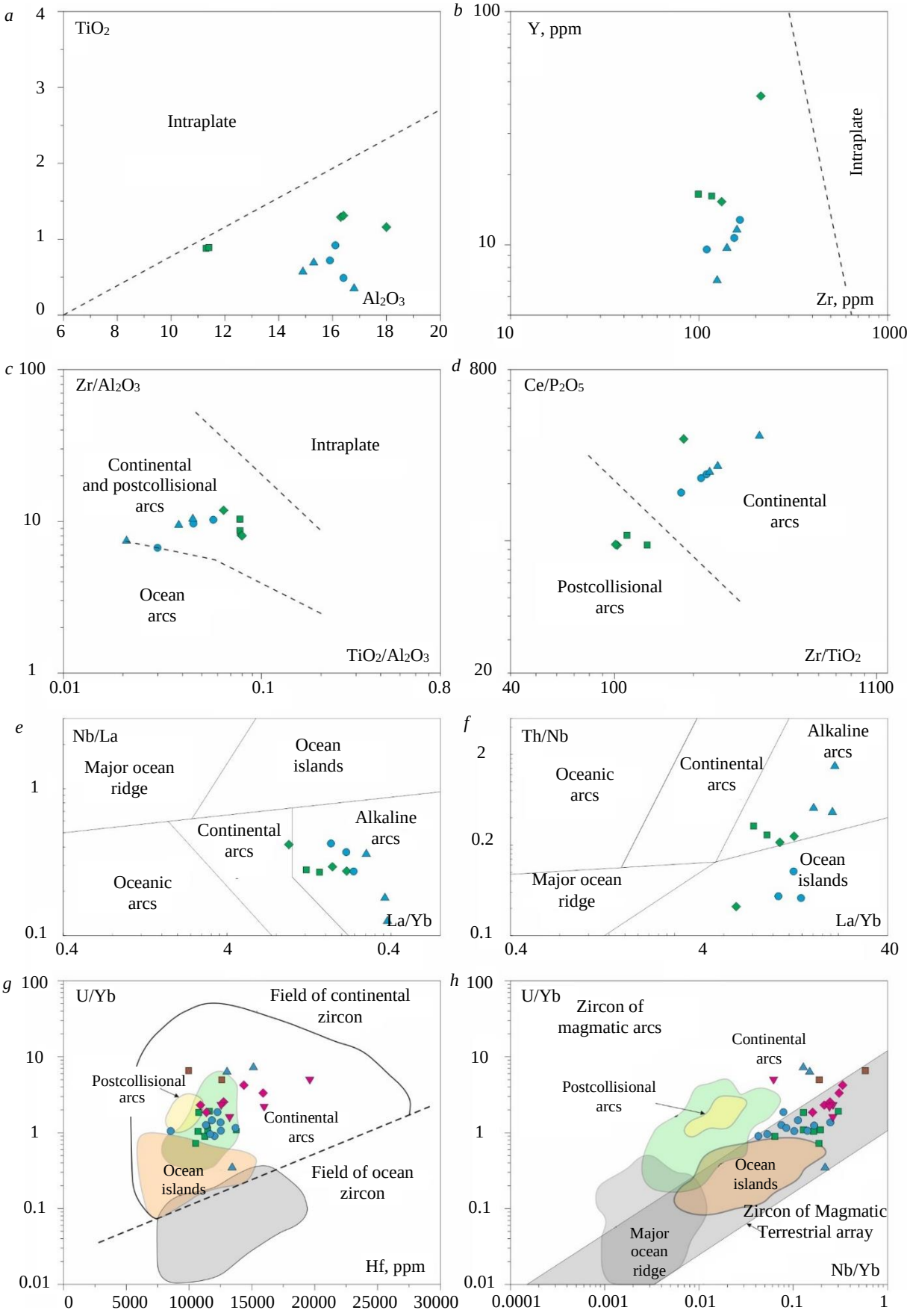


Fig.7. Diagrams of the geodynamic setting of the Saltakh Massif: *a-d* – after [19]; *e*, *f* – after [34]; *g*, *h* – diagrams of the geodynamic setting [54] of Saltakh Massif rocks after zircon composition. For symbols used, see Fig.5

This is an open access article under the CC BY 4.0 license

Age of metamorphism and anatexis. Earlier data for the Khapchan belt indicate that sedimentary deposits were fully metamorphosed 1.97 Ga ago and later subjected to areal granulite-facies metamorphism, peaking at 1.91-1.92 Ga ago [55]. Studies in the Billyakh tectonic zone [1] suggest that the Daldyn and Khapchan terrains collided between 1983±3 and 1971±4 Ma. While the current study does not recalculate the time of collisional metamorphism, available age dates indicate distinct pattern and sequence of metamorphic processes at the main stage of metamorphism.

Zircon from the dated samples reveals two types of metamorphic shells. Earlier zircon from the shells (1986±26 Ma), which appears white in CL, is poorly preserved and is usually surrounded by a later zircon rim (1971±10 Ma), which appears almost black in CL. These two types of zircon exhibit the contrasting geochemical characteristics of Th/U, Eu/Eu* and Ce/Ce* ratios. Modelling [26] indicates that the main factors affecting the Th/U value in suprasolidus metamorphic zircon include the Th and U concentrations in the system, as well as the destruction and growth of monazite or allanite, which are in equilibrium with zircon. Monazite and allanite, which are major Th-bearing phases growing alongside subsolidus zircon, decrease Th concentration and thus reduce Th/U [26]. Zircon, that formed during the early stages near the metamorphic peak, would show elevated Th/U values (e.g., white shells with Th/U = 0.51), whereas zircon that formed closer to the solidus line would display relatively low Th/U ratios (dark rims with Th/U = 0.08-0.13).

Zircon, which is white in CL, exhibits a higher Ce/Ce* = 19.8 and a better-defined negative Eu anomaly, (Eu/Eu* = 0.65), indicative of its formation in the plagioclase stability field under high oxygen fugacity conditions [56].

Zircon which is black in CL exhibits a positive Eu anomaly (Eu/Eu* = 1.54-2.92) but a weaker Ce anomaly (Ce/Ce* = 3.22-3.58), characteristic of a highly reducing setting. Besides, the positive Eu anomaly may result from the destruction of plagioclase (replacement of plagioclase by garnet and pyroxene), enriching the zircon crystallization medium in Eu. Similar to dark zircon shells, anatectic alaskitic gneissose granites (sample 673) also display well-defined positive Eu anomaly. However, both types of zircon display relatively high $(Lu/Gd)_N$ ratios: 28.8 in white zircon and 51.9-53.3 in black zircon, indicating the limited involvement of garnet in metamorphic paragenesis. This is likely due to the pattern of their protolith (mafic rocks), where pyroxene, rather than garnet, was formed under granulite-facies conditions.

The formation of alaskitic gneissose granites forming migmatite leucosome appears to be associated to the metamorphic peak. They exhibit high K_2O, La/Yb, and Sr/Y ratios, and positive Eu anomaly (Eu/Eu* = 12). This suggests partial rock melting provoked by potassium fluids resulted in the accumulation of cumulative plagioclase in the migmatite leucosome, which took place in equilibrium with garnet-granulite restite. The formation of leucogranites equilibrated with garnetiferous restite is possible at a temperature of 680 °C and a pressure of 11 kbar, with a high-water content [57]. The geochemical characteristics of alaskitic granites imply that plagioclase was involved in melting, provoking the Al, Sr, and Eu enrichment in the melt. The formation of alaskitic granites is linked to collision processes, with an excessively aquatic type of melting characteristic of collisional overthrusts, where a relatively cold inundated plate releases water into a hotter upper plate [57]. Paleoproterozoic granites of alaskitic type, associated with large lit-par-lit migmatite fields, are part of the Magan alaskitic-leucogranitic-migmatitic complex and are widespread in the Anabar Shield [55]. This suggests that the intensity of alaskitic-granitic magmatism is possibly related to collision processes. U-Pb dating indicates that the Magan complex was formed 1984-1952 Ma ago [55]. The zircon from alaskitic gneissose granites (sample 673) provides a concordant age of 1967±7 Ma.

This is an open access article under the CC BY 4.0 license

Conclusion

The Saltakh intrusive massif, composed of gabbro-diorite-tonalit, was metamorphosed under granulite-facies conditions and consists of two-pyroxene schists and plagiogneisses. Geochemical data indicate that it was formed by crystallization of calc-alkaline and shoshonitic magma in the near-continental magmatic arc extension conditions. Its isotopic-geochemical characteristics, including positive $\varepsilon_{Nd}(T)$ values ranging from +1.9 to +4.1 and fractionated HREE, suggest that the melt was formed at depth in equilibrium with a garnetiferous association. U-Pb zircon dating (SHRIMP II) reveals that Saltakh rocks intruded between 2100-2025 Ma ago from a deep source, which had a short crustal prehistory ($T_{(Nd)}DM$ = 2.20-2.26 Ga). The age of the metaintrusive Saltakh rocks is consistent with that of the Khapchan orthogranulites studied earlier [58], which are interpreted as part of a metamorphosed juvenile Paleoproterozoic suprasubduction complex.

REFERENCES

1. Smelov A.P., Kotov A.B., Salnikova E.B. et al. Age and duration of the formation of the Billyakh tectonic melange zone, Anabar shield. *Petrology*. 2012. Vol. 20. N 3, p. 286-300. DOI: 10.1134/S0869591112030058

2. Sukhanov M.K., Rachkov V.S. Saltakh massif of the Anabar shield. *Izvestiya Akademii nauk SSSR. Seriya geologicheskaya*. 1986. N 12, p. 47-58 (in Russian).

3. Lutts B.G., Oksman V.S. Deeply eroded fault zones of the Anabar shield. Moscow: Nauka, 1990, p. 259 (in Russian).

4. Williams I.S. U-Th-Pb Geochronology by Ion Microprobe. *Reviews in Economic Geology*. 1998. Vol. 7, p. 1-35. DOI: 10.5382/Rev.07

5. Black L.P., Kamo S.L., Allen C.M. et al. TEMORA 1: a new zircon standard for Phanerozoic U–Pb geochronology. *Chemical Geology*. 2003. Vol. 200. Iss. 1-2, p. 155-170. DOI: 10.1016/S0009-2541(03)00165-7

6. Fedotova A.A., Bibikova E.V., Simakin S.G. Ion-microprobe zircon geochemistry as an indicator of mineral genesis during geochronological studies. *Geochemistry International*. 2008. Vol. 46. N 9, p. 912-927. DOI: 10.1134/S001670290809005X

7. Skublov S.G., Levashova E.V., Mamykina M.E. et al. The polyphase Belokurikhinsky granite massif, Gorny Altai: isotope-geochemical study of zircon. *Journal of Mining Institute*. 2024. Vol. 268, p. 552-575.

8. Levashova E.V., Mamykina M.E., Skublov S.G. et al. Geochemistry (TE, REE, Oxygen) of Zircon from Leucogranites of the Belokurikhinsky Massif, Gorny Altai, as Indicator of Formation Conditions. *Geochemistry International*. 2023. Vol. 61. N 13, p. 1323-1339. DOI: 10.1134/S001670292311006X

9. Skublov S.G., Petrov D.A., Galankina O.L. et al. Th-Rich Zircon from a Pegmatite Vein Hosted in the Wiborg Rapakivi Granite Massif. *Geosciences*. 2023. Vol. 13. Iss. 12, p. 1-13. DOI: 10.3390/geosciences13120362

10. Levashova E.V., Skublov S.G., Oitseva T.A. et al. First Age and Geochemical Data on Zircon from Riebeckite Granites of the Verkhnee Espe Rare Earth–Rare Metal Deposit, East Kazakhstan. *Geochemistry International*. 2022. Vol. 60. N 1, p. 1-15. DOI: 10.1134/S0016702922010086

11. Rumyantseva N.A., Skublov S.G., Vanshtein B.G. et al. Zircon from Gabbroids of the Shaka Ridge (South Atlantic): U-Pb Age, Oxygen Isotope Ratios and Trace Element Composition. *Proceedings of the Russian Mineralogical Society*. 2022. Vol. 151. N 1, p. 44-73 (in Russian). DOI: 10.31857/S0869605522010099

12. Skublov S.G., Rumyantseva N.A., Li Qiuli et al. Zircon Xenocrysts from the Shaka Ridge Record Ancient Continental Crust: New U-Pb Geochronological and Oxygen Isotopic Data. *Journal of Earth Science*. 2022. Vol. 33. N 1, p. 5-16. DOI: 10.1007/s12583-021-1422-2

13. Adamskaya E.V., Badinova V.P., Belyatskii B.V. et al. Isotope geology of Norilsk deposits. St. Petersburg: VSEGEI, 2017, p. 348 (in Russian).

14. Jacobsen S.B., Wasserburg G.J. Sm-Nd isotopic evolution of chondrites and achondrites, II. *Earth and Planetary Science Letters*. 1984. Vol. 67. Iss. 2, p. 137-150.

15. Goldstein S.J., Jacobsen S.B. Nd and Sr isotopic systematics of river water suspended material: implications for crustal evolution. *Earth and Planetary Science Letters*. 1988. Vol. 87. Iss. 3, p. 249-265. DOI: 10.1016/0012-821X(88)90013-1

16. Whitney D.L., Evans B.W. Abbreviations for names of rock-forming minerals. *American Mineralogist*. 2010. Vol. 95. N 1, p. 185-187. DOI: 10.2138/AM.2010.3371

17. Hastie A.R., Kerr A.C., Pearce J.A., Mitchell S.F. Classification of Altered Volcanic Island Arc Rocks using Immobile Trace Elements: Development of the Th–Co Discrimination Diagram. *Journal of Petrology*. 2007. Vol. 48. Iss. 12, p. 2341-2357. DOI: 10.1093/petrology/egm062

18. O'Connor J.T. A classification for quartz-rich igneous rocks based on feldspar ratios. U.S. Geological Survey. Professional Paper 525-B. 1965, p. 79-84.

19. Müller D., Rock N.M.S., Groves D.I. Geochemical discrimination between shoshonitic and potassic volcanic rocks in different tectonic settings: A pilot study. *Mineralogy and Petrology*. 1992. Vol. 46. Iss. 4, p. 259-289. DOI: 10.1007/BF01173568

20. Pearce J.A. Trace element characteristics of lavas from destructive plate boundaries. Andesites. Orogenic Andesites and Related Rocks. John Wiley & Sons, 1982, p. 525-548.

21. de la Roche H., Leterrier J., Grandclaude P., Marchal M. A classification of volcanic and plutonic rocks using R_1R_2-diagram and major-element analyses – Its relationships with current nomenclature. *Chemical Geology*. 1980. Vol. 29. Iss. 1-4, p. 183-210. DOI: 10.1016/0009-2541(80)90020-0

This is an open access article under the CC BY 4.0 license

22. Peccerillo A., Taylor S.R. Geochemistry of eocene calc-alkaline volcanic rocks from the Kastamonu area, Northern Turkey. *Contributions to Mineralogy and Petrology*. 1976. Vol. 58. Iss. 1, p. 63-81. DOI: 10.1007/BF00384745

23. Irvine T.N., Baragar W.R.A. A Guide to the Chemical Classification of the Common Volcanic Rocks. *Canadian Journal of Earth Sciences*. 1971. Vol. 8. N 5, p. 523-548. DOI: 10.1139/e71-055

24. Ross P.-S., Bédard J.H. Magmatic affinity of modern and ancient subalkaline volcanic rocks determined from trace-element discriminant diagrams. *Canadian Journal of Earth Sciences*. 2009. Vol. 46. N 11, p. 823-839. DOI: 10.1139/E09-054

25. Sun S.-s., McDonough W.F. Chemical and isotopic systematics of oceanic basalts: implications for mantle composition and processes. *Geological Society, London, Special Publications*. 1989. Vol. 42, p. 313-345. DOI: 10.1144/GSL.SP.1989.042.01.19

26. Yakymchuk C., Kirkland C.L., Clark C. Th/U ratios in metamorphic zircon. *Journal of Metamorpic Geology*. 2018. Vol. 36. Iss. 6, p. 715-737. DOI: 10.1111/jmg.12307

27. Watson E.B., Harrison T.M. Zircon Thermometer Reveals Minimum Melting Conditions on Earliest Earth. *Science*. 2005. Vol. 308. Iss. 5723, p. 841-844. DOI: 10.1126/science.1110873

28. Hoskin P.W.O. Trace-element composition of hydrothermal zircon and the alteration of Hadean zircon from the Jack Hills, Australia. *Geochimica et Cosmochimica Acta*. 2005. Vol. 69. Iss. 3, p. 637-648. DOI: 10.1016/J.GCA.2004.07.006

29. Whitehouse M.J., Kamber B.S. On the overabundance of light rare earth elements in terrestrial zircons and its implication for Earth's earliest magmatic differentiation. *Earth and Planetary Science Letters*. 2002. Vol. 204. Iss. 3-4, p. 333-346. DOI: 10.1016/S0012-821X(02)01000-2

30. Bouvier A.-S., Ushikubo T., Kita N.T. et al. Li isotopes and trace elements as a petrogenetic tracer in zircon: insights from Archean TTGs and sanukitoids. *Contributions to Mineralogy and Petrology*. 2012. Vol. 163. Iss. 5, p. 745-768. DOI: 10.1007/s00410-011-0697-1

31. Grimes C.B., John B.E., Cheadle M.J. et al. On the occurrence, trace element geochemistry, and crystallization history of zircon from in situ ocean lithosphere. *Contributions to Mineralogy and Petrology*. 2009. Vol. 158. Iss. 6, p. 757-783. DOI: 10.1007/s00410-009-0409-2

32. Morrison G.W. Characteristics and tectonic setting of the shoshonite rock association. *Lithos*. 1980. Vol. 13. Iss. 1, p. 97-108. DOI: 10.1016/0024-4937(80)90067-5

33. Zindler A., Hart S. Chemical Geodynamics. *Annual Review of Earth and Planetary Sciences*. 1986. Vol. 14, p. 493-571. DOI: 10.1146/annurev.ea.14.050186.002425

34. Hollocher K., Robinson P., Walsh E., Roberts D. Geochemistry of Amphibolite-Facies Volcanics and Gabbros of the Støren Nappe in Extensions West and Southwest of Trondheim, Western Gneiss Region, Norway: A Key to Correlations and Paleotectonic Settings. *American Journal of Science*. 2012. Vol. 312. Iss. 4, p. 357-416. DOI: 10.2475/04.2012.01

35. Richards J.P., Spell T., Rameh E. et al. High Sr/Y Magmas Reflect Arc Maturity, High Magmatic Water Content, and Porphyry Cu ± Mo ± Au Potential: Examples from the Tethyan Arcs of Central and Eastern Iran and Western Pakistan. *Economic Geology*. 2012. Vol. 107. N 2, p. 295-332. DOI: 10.2113/econgeo.107.2.295

36. Ze Liu, Di-Cheng Zhu, Jagoutz O. et al. Magmatic Evolution following Damp Tholeiitic and Wet Calc-alkaline Liquid Lines of Descent: an Eastern Pontides (NE Turkey) Example. *Journal of Petrology*. 2021. Vol. 62. Iss. 5. N egaa088. DOI: 10.1093/petrology/egaa088

37. Jagoutz O., Schmidt M.W., Enggist A. et al. TTG-type plutonic rocks formed in a modern arc batholith by hydrous fractionation in the lower arc crust. *Contributions to Mineralogy and Petrology*. 2013. Vol. 166. Iss. 4, p. 1099-1118. DOI: 10.1007/s00410-013-0911-4

38. O'Brien T.M., Miller E.L. Continuous zircon growth during long-lived granulite facies metamorphism: a microtextural, U–Pb, Lu–Hf and trace element study of Caledonian rocks from the Arctic. *Contributions to Mineralogy and Petrology*. 2014. Vol. 168. Iss. 4. N 1071. DOI: 10.1007/s00410-014-1071-x

39. Rayner N., Stern R.A., Carr S.D. Grain-scale variations in trace element composition of fluid-altered zircon, Acasta Gneiss Complex, northwestern Canada. *Contributions to Mineralogy and Petrology*. 2005. Vol. 148. Iss. 6, p. 721-734. DOI: 10.1007/s00410-004-0633-8

40. Cavosie A.J., Valley J.W., Wilde S.A., E.I.M.F. Correlated microanalysis of zircon: Trace element, $\delta^{18}O$, and U–Th–Pb isotopic constraints on the igneous origin of complex > 3900 Ma detrital grains. *Geochimica et Cosmochimica Acta*. 2006. Vol. 70. Iss. 22, p. 5601-5616. DOI: 10.1016/j.gca.2006.08.011

41. Shao-Bing Zhang, Yong-Fei Zheng, Zi-Fu Zhao. Temperature effect over garnet effect on uptake of trace elements in zircon of TTG-like rocks. *Chemical Geology*. 2010. Vol. 274. Iss. 1-2, p. 108-125. DOI: 10.1016/j.chemgeo.2010.04.002

42. Whitehouse M.J., Kamber B.S. Assigning Dates to Thin Gneissic Veins in High-Grade Metamorphic Terranes: A Cautionary Tale from Akilia, Southwest Greenland. *Journal of Petrology*. 2005. Vol. 46. Iss. 2, p. 291-318. DOI: 10.1093/petrology/egh075

43. Pidgeon R.T., Nemchin A.A., Roberts M.P. et al. The accumulation of non-formula elements in zircons during weathering: Ancient zircons from the Jack Hills, Western Australia. *Chemical Geology*. 2019. Vol. 530. N 119310. DOI: 10.1016/j.chemgeo.2019.119310

44. Bell E.A., Boehnke P., Harrison T.M. Recovering the primary geochemistry of Jack Hills zircons through quantitative estimates of chemical alteration. *Geochimica et Cosmochimica Acta*. 2016. Vol. 191, p. 187-202. DOI: 10.1016/j.gca.2016.07.016

45. Skublov S.G., Lobach-Zhuchenko S.B., Guseva N.S. et al. Rare earth and trace element distribution in zircons from miaskite lamproites of the Panozero complex, Central Karelia. *Geochemistry International*. 2009. Vol. 47. N 9, p. 901-913. DOI: 10.1134/S0016702909090043

46. Stevenson R., Henry P., Gariépy C. Assimilation–fractional crystallization origin of Archean Sanukitoid Suites: Western Superior Province, Canada. *Precambrian Research*. 1999. Vol. 96. Iss. 1-2, p. 83-99. DOI: 10.1016/S0301-9268(99)00009-1

47. Lobach-Zhuchenko S.B., Rollinson H.R., Chekulaev V.P. et al. The Archaean sanukitoid series of the Baltic Shield: geological setting, geochemical characteristics and implications for their origin. *Lithos*. 2005. Vol. 79. Iss. 1-2, p. 107-128. DOI: 10.1016/j.lithos.2004.04.052

48. Lobach-Zhuchenko S.B., Rollinson H., Chekulaev V.P. et al. Petrology of a Late Archaean, Highly Potassic, Sanukitoid Pluton from the Baltic Shield: Insights into Late Archaean Mantle Metasomatism. *Journal of Petrology*. 2008. Vol. 49. Iss. 3, p. 393-420. DOI: 10.1093/petrology/egm084

This is an open access article under the CC BY 4.0 license

49. Pe-Piper G., Piper D.J.W., Koukouvelas I. et al. Postorogenic shoshonitic rocks and their origin by melting underplated basalts: The Miocene of Limnos, Greece. *GSA Bulletin*. 2009. Vol. 121. N 1-2, p. 39-54. DOI: 10.1130/B26317.1

50. Solovev S.G. Metallogeny of Shoshonitic magmatism. In 2 volumes. Vol. 1. Moscow: Nauchnyi mir, 2014, p. 528 (in Russian).

51. Meen J.K. Formation of shoshonites from calcalkaline basalt magmas: geochemical and experimental constraints from the type locality. *Contributions to Mineralogy and Petrology*. 1987. Vol. 97. Iss. 3, p. 333-351. DOI: 10.1007/BF00371997

52. de Astis G., Ventura G., Vilardo G. Geodynamic significance of the Aeolian volcanism (Southern Tyrrhenian Sea, Italy) in light of structural, seismological, and geochemical data. *Tectonics*. 2003. Vol. 22. Iss. 4. N 1040. DOI: 10.1029/2003TC001506

53. Carminati E., Lustrino M., Doglioni C. Geodynamic evolution of the central and western Mediterranean: Tectonics vs. igneous petrology constraints. *Tectonophysics*. 2012. Vol. 579, p. 173-192. DOI: 10.1016/j.tecto.2012.01.026

54. Grimes C.B., Wooden J.L., Cheadle M.J., John B.E. «Fingerprinting» tectono-magmatic provenance using trace elements in igneous zircon. *Contributions to Mineralogy and Petrology*. 2015. Vol. 170. Iss. 5-6. N 46. DOI: 10.1007/s00410-015-1199-3

55. Gusev N.I. Anabar shield of the Siberian Craton: composition, geochemistry, geochronology. Saarbrucken: LAP LAMBERT Academic Publishing, 2013, p. 188.

56. Trail D., Watson E.B., Tailby N.D. Ce and Eu anomalies in zircon as proxies for the oxidation state of magmas. *Geochimaca et Cosmochimica Acta*. 2012. Vol. 97, p. 70-87. DOI: 10.1016/j.gca.2012.08.032

57. Frost C.D., Swapp S.M., Frost B.R. et al. Leucogranites of the Teton Range, Wyoming: A record of Archean collisional orogeny. *Geochimica et Cosmochimica Acta*. 2016. Vol. 185, p. 528-549. DOI: 10.1016/j.gca.2015.12.015

58. Gusev N.I., Sergeeva L.Y., Skublov S.G. Evidence of Subduction of the Paleoproterozoic Oceanic Crust in the Khapchan Belt of the Anabar Shield, Siberian Craton. *Petrology*. 2021. Vol. 29. N 2, p. 95-113. DOI: 10.1134/S0869591121020041

***Authors*: Nikolai I. Gusev,** *Head of Department, https://orcid.org/0000-0002-3461-0961* (*Karpinsky Russian Geological Research Institute, Saint Petersburg, Russia*; *Institute of Precambrian Geology and Geochronology RAS, Saint Petersburg, Russia*), **Lyudmila Yu. Romanova,** *Candidate of Geological and Mineralogical Sciences, Leading Engineer, sergeeva.luda02@yandex.ru, https://orcid.org/0009-0005-2766-0097* (*Karpinsky Russian Geological Research Institute, Saint Petersburg, Russia*; *Institute of Precambrian Geology and Geochronology RAS, Saint Petersburg, Russia*).

The authors declare no conflict of interests.

This is an open access article under the CC BY 4.0 license